

# A comparison of chemistry and dust cloud formation in ultracool dwarf model atmospheres

Ch. Helling,<sup>1\*</sup>, A. Ackerman<sup>2</sup>, F. Allard<sup>3,4</sup>, M. Dehn<sup>5</sup>, P. Hauschild<sup>5</sup>, D. Homeier<sup>6</sup>, K. Lodders<sup>7</sup>, M. Marley<sup>8</sup>, F. Rietmeijer<sup>9</sup>, T. Tsuji<sup>10</sup>, P. Woitke<sup>11</sup>

<sup>1</sup> SUPA, School of Physics and Astronomy, Univ. of St Andrews, North Haugh, St Andrews, KY16 9SS, UK

<sup>2</sup> NASA Goddard Institute of Space Studies, New York, New York, USA

<sup>3</sup> Centre de Recherche Astrophysique de Lyon, CNRS, UMR5574, Université de Lyon, Ecole Normale Supérieure de Lyon, 47 Allée d'Italie, F-69634 Lyon, France

<sup>4</sup> Institut d'Astrophysique de Paris, CNRS, UMR 7095, 98<sup>bis</sup> Boulevard Arago, F-75014 Paris, France

<sup>5</sup> Hamburger Sternwarte, Gojenbergsweg 112, 21029 Hamburg, Germany

<sup>6</sup> Georg-August-Universität Göttingen, Institut für Astrophysik, Friedrich-Hund-Platz, 137077 Göttingen, Germany

<sup>7</sup> Planetary Chemistry Laboratory, Department of Earth and Planetary Science, Washington University, St. Louis, MO, 63130

<sup>8</sup> NASA Ames Research Center, MS 254-3, Moffett Field, CA 94035

<sup>9</sup> Department of Earth and Planetary Sciences, MSC03-2040, University of New Mexico, Albuquerque, NM 87131-0001, USA

<sup>10</sup> Institute of Astronomy, The University of Tokyo, 2-21-1 Osawa, Mitaka, Tokyo, 181-0015 Japan

<sup>11</sup> UK Astronomy Technology Center, Royal Observatory, Blackford Hill, Edinburgh EH9 3HJ, Scotland, UK

Accepted . Received ; in original form 2008 month day

## ABSTRACT

The atmospheres of substellar objects contain clouds of oxides, iron, silicates, and other refractory condensates. Water clouds are expected in the coolest objects. The opacity of these ‘dust’ clouds strongly affects both the atmospheric temperature-pressure profile and the emergent flux. Thus any attempt to model the spectra of these atmospheres must incorporate a cloud model. However the diversity of cloud models in atmospheric simulations is large and it is not always clear how the underlying physics of the various models compare. Likewise the observational consequences of different modelling approaches can be masked by other model differences, making objective comparisons challenging. In order to clarify the current state of the modelling approaches, this paper compares five different cloud models in two sets of tests. Test case 1 tests the dust cloud models for a prescribed L, L–T, and T-dwarf atmospheric (temperature  $T$ , pressure  $p$ , convective velocity  $v_{\text{conv}}$ )-structures. Test case 2 compares complete model atmosphere results for given (effective temperature  $T_{\text{eff}}$ , surface gravity  $\log g$ ). All models agree on the global cloud structure but differ in opacity-relevant details like grain size, amount of dust, dust and gas-phase composition. These models can loosely be grouped into *high-* and *low-altitude cloud* models whereas the first appear generally redder in near-infrared colours than the later. Comparisons of synthetic photometric fluxes translate into an modelling uncertainty in apparent magnitudes for our L-dwarf (T-dwarf) test case of  $0.25 \lesssim \Delta m \lesssim 0.875$  ( $0.1 \lesssim \Delta m \lesssim 1.375$ ) taking into account the 2MASS, the UKIRT WFCAM, the Spitzer IRAC, and VLT VISIR filters with UKIRT WFCAM being the most challenging for the models. Future developments will need closer links with laboratory astrophysics, and a consistent treatment of the cloud chemistry and turbulence.

**Key words:** Stars: atmospheres – Stars: low-mass, brown dwarfs

## 1 INTRODUCTION

The atmospheres of L dwarfs are characterised by clouds, formed principally of silicate, oxide and iron grains, which shape their emergent spectra. Likewise the atmospheres of the early T dwarfs are distinguished by the progressive departure of cloud opacity. At even lower effective temperature, giant-gas planets are again

covered in clouds and other chemical components become important. Any attempt to derive fundamental properties of these objects from their spectra hinges on an understanding of the chemistry and physics of clouds. Yet clouds are inherently difficult to model since they can feedback into the chemistry and the physics of the entire atmosphere. Because of the complexity of this problem a number of independent groups have taken very different approaches to describe the cloud formation and the cloud properties of substellar objects as a function of gravity, effective temperature, and metal-

\* E-mail: Christiane.Helling@st-and.ac.uk

licity. Here we make a first attempt to compare the quantitative predictions of these various approaches in order to better understand the models themselves as well as the uncertainty which remains in application of these models to real objects.

Atmospheric physics classically involves hydrodynamics, radiative and convective energy transport, and gas phase chemistry. Effects of magnetic fields are neglected. Ideally, the only free parameters are the effective temperature  $T_{\text{eff}}$ , the surface gravity  $g$ , radius  $R_*$  or mass  $M_*$ , and element abundances  $\epsilon_i$ . In order to solve such a coupled system of equations in a computationally reasonable time, assumptions like the hydrostatic equilibrium, mixing length theory and chemical equilibrium are made. Inside substellar atmospheres, chemical equilibrium of the gas phase is justified due to high collision rates between gas-phase constituents. Irradiation or atmospheric flows may invalidate this assumption in the upper atmospheric layers. The validity of hydrostatic equilibrium and mixing length theory have been studied in comparison to large eddy simulations for M-type stars (Ludwig et al. 2002, 2006) and we know from the direct observation of solar system giant planets at low gravities and effective temperatures that hydrostatic equilibrium is an appropriate down to very low pressures ( $\sim 1 \mu\text{bar}$ ) in the atmosphere. The assumption of hydrostatic equilibrium coupled with the mixing length theory is computationally extremely efficient and an accurate approximation in particular if one is aiming at synthetic spectrum calculations.

The striking difference of substellar atmosphere models compared to the classical stellar approach is the necessity to model the formation of clouds and their feedback onto the entire atmosphere. New physics needed to be considered and different tribes emerged being inspired by AGB star dust formation (Helling et al. 2001a; Woitke & Helling 2003, 2004), by terrestrial cloud formation (Ackerman & Marley 2001, Cooper et al. 2003), by measurements for solar system planets (Rossow 1978, Marley et al. 1999), or driven by practical considerations (Tsuji et al. 1996 a,b; Allard et al. 2001). The first attempts on cloud modelling in brown dwarf atmospheres were undertaken by Lunine, Hubbard & Marley (1986) and Tsuji et al. (1996 a,b) who suggested the influence of clouds on the spectral appearance of brown dwarfs. See also Ackerman & Marley (2001) for a review and comparison of the earlier cloud literature.

The overall, phenomenological understanding of cloud formation in substellar objects has converged to the picture that dust (or condensates, see Table 3) forms at a certain height in the atmosphere where it acts as an efficient element sink leaving behind a depleted gas phase. The departure of TiO and FeH spectral lines from the M to the L dwarfs testifies to this process. The dust then settles gravitationally taking condensed elements with it. Convection and atmospheric mixing replenishes the condensing gas, resulting in a steady state. The details of this picture, however, leave room for debate. It is for example not clear where the dust precisely starts to form since this depends on the details of the model assumptions.

Current models generally employ one of two physical approaches to understand this process. In the first paradigm gas is mixed upward into higher altitudes. Dust then forms, falls down and meanwhile grows until it evaporates below the cloud base (Woitke & Helling 2003). The second paradigm imagines the opposite limiting case in which the gas is well mixed from the deep atmosphere only up to a cloud base. Grains and gas are transported above cloud base by mixing and grains fall down under the influence of gravity (Ackerman & Marley 2001, Allard et al. 2003). These two branches rely on fundamentally different model assump-

tions: (i) the phase-non-equilibrium concept of kinetic dust formation (Woitke & Helling 2003, 2004; Helling & Woitke 2006, Helling, Woitke & Thi 2008), and (ii) the phase-equilibrium concept of thermal stability (Tsuji et al. 1996b, Tsuji 2005, Allard et al. 2001, Ackerman & Marley 2001, Burrows et al. 2006; Cooper et al. 2003). While (ii) represents the end-state which a dust forming system achieves for  $t \rightarrow \infty$ , (i) describes the kinetic process of the formation of cloud particles on finite timescales limited by mixing and rain-out. The models also differ in the choice of dust materials which are assumed (i) to form or (ii) to be present in the atmosphere. Both areas need serious attention and corresponding material properties should be obtained either experimentally (see discussion Sect. 4) or from ab initio calculation (e.g. Jeong et al. 2000, Patzer et al. 2005) which both are beyond the scope of this paper. Given these model conceptions, a number of different model approaches have been developed to reproduce observed spectra (Tsuji et al. 1996a, Tsuji 2005, Allard et al. 2001, Ackerman & Marley 2001, Burrows et al. 2006, Cooper et al. 2003, Dehn 2007, Helling et al. 2008a,b) or providing detailed information on the dust complex itself (Woitke & Helling 2003, 2004; Helling & Woitke 2006, Helling, Woitke & Thi 2008).

Driven by this diversity in the field, the aim of this paper is to provide information and to perform comparative studies of models that aim to describe the dust clouds in substellar atmospheres. Kleb & Wood (2004) demonstrated that such component-based test studies are an essential part of scientific methods. As the number,  $n$ , of model components increases, the interactions amongst them grow as  $n^2/2$ . We therefore need to perform verifications on the components (here: cloud models) but also to use the method of *manufactures solutions*<sup>1</sup> (e.g. Kleb & Wood 2004) to verify that the entire system (here: model atmosphere) attains its theoretical order-of-accuracy properties. This goes beyond what has been and could be provided in the literature so far.

Our paper begins with a summary of the various dust cloud models. We provide for the first time a comparative presentation of the different approaches concerning chemistry and dust modelling (Sect. 2). Based on a workshop held in Leiden in October 2006 (<sup>2,3</sup>), we present test cases where we first separate the components for chemistry and dust cloud modelling from the complete atmosphere problem (Sect. 3.1). This allows us to judge the order-of-accuracy properties of the complete models with respect to chemistry and dust formation which both are essential ingredients for the solution of the radiative transfer problem. Section 3.3 demonstrates the results for the complete substellar atmosphere problem, synthetic photometric fluxes, and colours are calculated and synthetic trust ranges derived from independent models are given.

Comparative studies have been carried out for simulations of radiative transfer (Pascucci et al. 2004, Iliev et al. 2006), of white dwarfs (Barstow et al. 2001) or photon dominated region (Röllig et al. 2007). No comparison study has been presented so far for substellar atmospheres (brown dwarfs and planets). While we compare a number of model predictions, including emergent spectra, we refrain from comparing against spectra of individual substellar objects, since there are as yet no such objects with independently

<sup>1</sup> *Manufactures solutions* are tests with a known results. In our case, we manufacture the input quantities to a certain extent and compare the solutions (test case 1, Sect.3.1).

<sup>2</sup> <http://www.lorentzcenter.nl/lc/web/2006/203/info.php3?wsid=203>

<sup>3</sup> <http://phoenix.hs.uni-hamburg.de/BrownDwarfsToPlanets1/>

**Table 1.** Definition and units of quantities. The quantities plotted in Figs. 1–9 are highlighted in **boldface**.

Quantity	Definition	Unit
$T$	<b>local gas temperature</b> (Fig. 1, 5)	K
$p_{\text{gas}}$	<b>local gas pressure</b>	dyn cm <sup>-2</sup>
$v_{\text{conv}}$	<b>convective velocity</b>	cm s <sup>-1</sup>
$\epsilon_i$	gas element abundance (i = H, He, ...)	
$\epsilon_i^0$	deep element abundance	
$S$	supersaturation ratio	
$\rho_d/\rho_{\text{gas}}$	<b>dust to gas mass ratio</b> (Fig. 2)	
$\rho_d$	dust mass density	g cm <sup>-3</sup>
	$= \sum_s n_s M_s$ for $a = \text{const}$	
	$= \sum_s \int_a f(a) M_s(a) da$	
$s$	dust species (e.g. Fe[s], Mg <sub>2</sub> SiO <sub>4</sub> [s], ...)	
$n_s$	number of dust particles of kind $s$	cm <sup>-3</sup>
$a$	grain size	cm
$M_s$	mass of dust particle of kind $s$	g
$f(a)$	grain size distribution: number of dust grains $n$ per grain size $a$ and per gas volume	cm <sup>-3</sup> cm <sup>-1</sup>
$\langle a \rangle$	<b>mean particle size</b> (Fig. 2)	cm
	$= \frac{\sum_s \int_a f_s(a) a da}{\sum_s \int_a f_s(a) da}$	
	for fixed $a = a_0$ : $f(a) = \delta(a - a_0) \Rightarrow \langle a \rangle = a_0$	
$V_s/V_{\text{tot}}$	<b>volume fraction of dust kind <math>s</math></b> (Fig. 3)	1
$V_s$	total dust volume of dust kind $s$	cm <sup>3</sup>
$V_{\text{tot}}$	total dust volume	cm <sup>3</sup>
$F(\lambda)$	<b>surface flux</b> (Fig. 6, 7)	erg s <sup>-1</sup> cm <sup>-2</sup> Å <sup>-1</sup>
$\lambda$	wavelength	μm
$\log F_c$	<b>photometric flux</b> (Fig. 8)	erg s <sup>-1</sup> cm <sup>-2</sup> Å <sup>-1</sup>
	flux convolved with filter $c$	
	$= \frac{\int_{\lambda_1}^{\lambda_2} F(\lambda) \text{trans}_c(\lambda) d\lambda}{\int_{\lambda_1}^{\lambda_2} \text{trans}_c(\lambda) d\lambda}$	
$\log F_{c0}$	reference photometric flux (Vega)	
$\text{trans}_c(\lambda)$	function of a photometric filter $c$ between $\lambda_1$ and $\lambda_2$ (see Table 6)	
$m_1 - m_2$	<b>colour</b> (Fig. 9)	
	$= 2.5 \left( \log \frac{F_{c2}(\Delta\lambda_2)}{F_{c02}(\Delta\lambda_2)} - \log \frac{F_{c1}(\Delta\lambda_1)}{F_{c01}(\Delta\lambda_1)} \right)$	
$m$	apparent magnitude	
	$= -2.5 \log \int_{\lambda_1}^{\lambda_2} F(\lambda) \text{trans}_c d\lambda$	

constrained mass, age, and metallicity against which spectral models can be compared.

## 2 APPROACHES TO CHEMISTRY AND DUST CLOUD MODELLING IN BROWN DWARF ATMOSPHERES

### 2.1 Gas phase chemistry

Each of the cloud models to be summarised (Sect. 2.2) assumes local thermodynamic equilibrium (LTE) when modelling the gas phase chemistry. In stellar atmospheres, departures from LTE can arise from interactions of atoms and molecules with the non-thermal radiation field (Woitke, Krüger & Sedlmayr 1996) but this effect is negligible in dense substellar atmospheres (Hauschildt et al. 1997; Schweitzer, Hauschildt & Baron 2000). Dust and gas are

assumed to have the same temperature ( $T_{\text{dust}} = T_{\text{gas}}$ ). The gas phase abundances determine the kind and the amount of dust condensing and are in turn determined by the amount of elements not bound by the dust. All codes use equilibrium constants  $K_p$  in their gas-phase treatments (Fegley & Lodders 1994; Tsuji et al. 1996b, Tsuji 2005; Allard et al. 2001, 2003; Lodders 2003; Helling & Woitke 2006; Helling, Woitke & Thi 2008). In reality, differences may arise due to the selection of the input data, which would be apparent in direct comparisons among the various gas-phase models.

The aim of this paper is to investigate and quantify the differences arising from different cloud model approaches rather than testing thermodynamic data sources. While we do not expect large uncertainties due to possible difference in thermodynamical gas-phase data, the results of the gas-phase chemistries used by different modellers will differ if different sources for element abundances were used (see discussion in Sect. 3.1).

### 2.2 Dust cloud models

In the following we summarise five different cloud models which are used in substellar atmosphere simulations, and which are involved in our comparative calculations (Sect. 3.2, 3.4). While there are many differences, ultimately all of the models face the same underlying physical challenges. We will try to note conceptual similarities and differences as we describe the models below.

The descriptions include where appropriate:

- the link between the cloud module and the atmosphere code,
- the physical ideas and their representation,
- the treatment of the cloud chemistry.

#### 2.2.1 Tsuji model

**2.2.1.1 Dust and gas-phase treatment in model atmosphere code:** Tsuji and collaborators apply the methods of non-grey radiative transfer (in hydrostatic and radiative-convective equilibrium under LTE) to dusty photospheres with almost no modification, except that the solid and liquid phases are considered in addition to the gas phase in chemical equilibrium. In solving chemical equilibrium, the Tsuji models aim to provide the abundances of ions, atoms, molecules, and dust grains that contribute to the opacities rather than to derive a complete solution for all elements. Thirty-four elements are considered in charge conservation, 16 elements (H, C, N, O, Na, Mg, Al, Si, P, S, Cl, K, Ca, Ti, V, Fe) in molecular formation, and 8 elements (Mg, Al, Si, Fe, K, Ca, Ti, V) in dust formation. The chemical equilibrium computation includes 83 molecules and is based on a previous examination of about 500 molecular species (as for details, including the thermochemical data, see Tsuji 1973). Dust grains composed of Fe, Si, Mg, and Al in form of metallic iron, enstatite (MgSiO<sub>3</sub>), and corundum (Al<sub>2</sub>O<sub>3</sub>) are considered as sources of dust opacity. The abundances are solved as being in phase equilibrium with gaseous species. No other dust species composed of Fe, Si, Mg, or Al are considered for simplicity. Also, abundances of some gaseous species important as sources of gaseous opacity suffer large reduction by the dust formation, and such effects are approximated by perovskite (CaTiO<sub>3</sub>) for Ti, melilite (Ca<sub>2</sub>MgSi<sub>2</sub>O<sub>7</sub>) for Ca, VO(cr) for V, and K<sub>2</sub>S(cr)/KCl(cr) for K, since gaseous TiO, CaH, VO, and K are important sources of gas opacity.

**Table 2.** Dust cloud models in substellar atmospheres ( $z$  - atmospheric height;  $s$  - dust species).

The references are the following: ① – Tsuji (2000); ② – Tsuji et al. (1996b); ③ – Tsuji (2002, 2005), ④ – Allard et al. (2001); ⑤ – Allard et al. (2003); ⑥ – Ackerman & Marley (2001), ⑦ – Woitke & Helling (2003), Helling, Woitke & Thi (2008)

Author	Assumptions			Model variants		
	grain size $a$	grain composition	supersaturation			references
Tsuji	$a = 10^{-2} \mu\text{m}$	homogeneous	$S = 1$	<i>case B</i>	full dusty model	①
				<i>case C</i>	dust cleared model	②
				<i>UCM</i>	dust between	③
					$T_{\text{cr}} < T < T_{\text{cond}}$	
Allard & Homeier	$f(a) = a^{-3.5}$ (ISM)	homogeneous	$S = 1$	<i>dusty</i>	full dusty model	④
	time scale comparison ( $\nearrow$ Rossow 1978)	homogeneous	$S = 1.001$	<i>cond</i>	dust cleared model	④
				<i>settl</i>		⑤
Ackerman & Marley	log-normal $f(a, z)$	homogeneous	$S = 1$	$f_{\text{sed}}$	sedimentation efficiency	⑥
Helling & Woitke	$f(a, z)$	dirty	$S = S(z, s)$			⑦

**2.2.1.2 Cloud model:** The Tsuji models assume that dust forms in the photosphere as soon as the thermodynamical condition for condensation is met, i.e. the supersaturation  $S = 1$ . Then the layers cooler than the condensation temperature ( $T_{\text{cond}}$ ) are assumed to be filled with dust grains (*case B*) which act as element sink and opacity source. Another extreme case is that the dust grains all precipitate as soon as they are formed and the atmosphere is thus clear of dust (*case C*), hence the dust acts as element sink but not as opacity source. Finally an intermediate case (the “Unified” or UCM case) in which grains condense at  $T_{\text{cond}}$ , but precipitate at a slightly lower temperature termed the critical temperature,  $T_{\text{cr}}$  is also considered. In this case the dust cloud appears in a restricted region of  $T_{\text{cr}} < T < T_{\text{cond}}$ .

While  $T_{\text{cond}}$  is well defined by thermal stability,  $T_{\text{cr}}$  is left as a free parameter to be estimated empirically. If  $T_{\text{cr}}$  is equal to  $T_{\text{cond}}$ , all the dust grains will precipitate as soon as they are formed (*case C*). On the other hand, if  $T_{\text{cr}}$  is as low as the surface temperature, all the dust grains formed will survive in the fully dusty photosphere (*case B*). If  $T_{\text{cr}}$  differs only slightly from  $T_{\text{cond}}$ , the dust cloud will be quite thin while the dust cloud will be rather thick if  $T_{\text{cr}}$  is much lower than  $T_{\text{cond}}$ . Thus  $T_{\text{cr}}$  is essentially a measure of the thickness of the dust cloud and thus has a significant effect on the infrared colours (not unlike  $f_{\text{sed}}$  in the Ackerman & Marley (2001) model). As a free parameter  $T_{\text{cr}}$  (along with  $T_{\text{eff}}$ ) can be inferred from the observed infrared colours. For this purpose, reasonably accurate values of  $T_{\text{eff}}$  can be inferred from the luminosities based on the observed parallaxes and bolometric fluxes (e.g. Golimowski et al. 2004; Vrba et al. 2004). But it appeared that the infrared colours differ significantly even for the same  $T_{\text{eff}}$  (e.g. Marley et al. 2005; Tsuji 2005) and this fact implies that  $T_{\text{cr}}$  also differs for the same  $T_{\text{eff}}$ . For example, four cool dwarfs from spectral type L6.5 to T3.5, whose infrared spectra are quite different, appear to have almost the same empirical  $T_{\text{eff}}$  at about  $1400 \pm 100$  K. Such very different spectra of almost the same  $T_{\text{eff}}$  could be explained reasonably well by assuming different values of  $T_{\text{cr}}$ , i.e. different thickness of the dust cloud (see Fig. 10 of Tsuji 2005).

In the Tsuji models all grains have radius  $a = 0.01 \mu\text{m}$ . In the limit of such small sizes the dust opacity is independent of the particle size for a fixed mass of dust.

## 2.2.2 Allard & Homeier model

### 2.2.2.1 Dust and gas-phase treatment in model atmosphere

**code:** The Allard & Homeier models solve for chemical equilibrium in the gas phase by minimisation of the functional errors, where the functions are the elemental and charge conservation, Saha equation, and mass-action law for each of 40 elements, with up to 5 ionisation levels per atom, and for some 600 molecules and nearly as many condensate using thermochemical data from many sources including a compilation of the JANAF tables (Chase et al. 1986; for details see Allard et al. 2001 and Allard & Hauschildt 1995).

Allard et al. (2001) modelled the limiting effects of cloud formation (*dusty*, *cond*) on the spectral properties of late M and L to T brown dwarfs by treating dust in chemical equilibrium with the gas phase. For the grains construction and opacities in the *dusty* and the *cond* models, an interstellar size distribution of spherical and chemical homogeneous grains is assumed. A slight supersaturation (1.001) is assumed in the *settl* models (Allard et al. 2003, 2007).

The grain sizes are calculated from the comparisons between time-scales for mixing due to convective overshooting as prescribe by (Ludwig et al. 2002) and condensation and gravitational settling according to Rossow (1978). The thermal structure of the model atmosphere is solved on a fixed optical depth grid at  $1.2 \mu\text{m}$  assuming no dust opacity contribution. The *dusty* models accounted for dust opacity while the *cond* models did not (Allard et al. 2001). The *settl* models involve a detailed cloud model (Allard et al. 2003, 2007) which is solved for the thermal structure of the atmosphere to find the grain size and abundances distributions as function of depth. In order to account for the gas cooling effects as it is propelled by convective turbulence from the top of the convection zone towards the top of the atmosphere, the cloud model is solved by depleting gas phase abundances layer-by-layer from the innermost (assumed of solar composition) to the outermost layer.

The resulting stratified elemental abundances and number densities of species are then used in the radiative transfer solver applying the Mie equation and complex refractive index for calculating the dust opacities (Ferguson et al. 2005). Models are converged removing thereby any possible cloud opacity inconsistencies between thermal structure and radiative transfer.

**2.2.2.2 Cloud model:** For the *settl* model atmosphere (Allard et al. 2003, 2007) in each layer, the condensation, sedimentation and

**Table 3.** A brief dictionary for multiple meanings and phrases (a, b, ...) used by different authors (T - Tsuji; AH - Allard & Homeier; MAL - Marley, Ackerman & Lodders; HW - Helling & Woitke; R - Rietmeijer).

dust	a) (HW)	general term for small solid particles, grains, liquid droplets
	b) (MAL)	condensate
condensation	a) (T, AH)	dust formation by conversion of vapour to solid (or liquid) particles
nucleation	a) (MAL, HW)	seed particle formation
growth	a) (HW)	formation of condensate species by chemical surface reaction on an existing surface
evaporation	a) (HW)	reverse growth process ( $\tau_{\text{evap}}$ - evaporation time scale)
drift	a) (HW)	relative motion between gas and dust
	b) (MAL)	gravitational settling
	c) (MAL)	rain, rain-out
	d) (AH, MAL)	sedimentation: the falling of cloud particles under the influence of gravity ( $\tau_{\text{sed}}$ - sedimentation time scale)
	e) (T, MAL)	precipitation: formation of cloud particle for which $\tau_{\text{evap}} \gg \tau_{\text{sed}}$ (from Rossow 1978)
homogeneous nucleation	a) (HW)	seed formation by addition of the same monomer species forming clusters of increasing sizes until they achieve solid state character
	b)	formation of first condensate that will grow to increasingly larger clusters
heterogeneous nucleation	a)	seed formation by addition of different monomer species
	b) (R)	formation of condensed species onto an existing seed ( $\nearrow$ growth)
primary condensate	a) (MAL)	a condensate forming from the gas by gas-gas reactions
secondary condensate	a) (MAL)	a condensate forming by gas-solid reaction with previously existing solid or liquid phase
coagulation	a)	formation of one particle from two colliding cloud particles
coalescence	a) (AH)	coagulation caused by size dependent sedimentation velocities of cloud particles of different sizes
element conservation		exchangeable used with mass balance since no elements should be created inside the atmosphere
supersaturation	a) (HW, T, AH)	$S$ , the ratio of the monomer particle pressure to the saturation vapour pressure (see Helling, Woitke & Thi 2006, Appendix for discussion)
	b) (MAL)	$S - 1$ , the vapour pressure in excess of saturation divided by the saturation vapour pressure

coalescence timescales (Rossow 1978; see Table 3) are compared to the mixing timescale prescribed by Ludwig et al. (2002) as follows:

- the equilibrium size between mixing and sedimentation is calculated and the growth time scale (condensation and coalescence) is computed for that size;
- the mixing time scale is then compared to the growth time scale:

- if growth is faster the condensates are found to be depleted, and the fraction of condensates is recomputed so as to obtain a growth time scale equal to the mixing time scale;
- when mixing is faster, the growth is limited by the replenishment with fresh condensable material from deeper layers, and, while the condensate fraction is stable, a mean size is recomputed corresponding to an equilibrium between mixing and condensation.

Given the new cloud description the elemental abundances are then readjusted which produces a new equilibrium condensate fraction. These steps are repeated until the condensate fraction no longer changes. This is a time consuming process which however guaranties that the chemistry reflects the cooling path of the gas.

Another essential input to the model is the description of the mixing timescale. Within the lower classically convective unstable atmosphere layers a mixing velocity is readily obtained from the results of mixing length theory, which is implemented in PHOENIX in the formulation of Mihalas (1978). Since the principal cloud formation region is located well above the Schwarzschild boundary, one is confronted with the task of extrapolating the velocities over several pressure scale heights. For a phenomenological description of this velocity field this group draws on the results of the hydrodynamical simulations of late M dwarfs by Ludwig et al. (2002), which show in general an exponential decline of mass transfer by

overshooting with decreasing pressure, after an initial transition zone. Further simulations by Ludwig (2003) indicate a steepening of this decline with surface gravity. The mass exchange frequency following these simulations is parameterised in analogy to the Helling & Woitke -model as  $\log \tau_{\text{mix}}(z) = \log \tau_{\text{MLT}} + \beta(\log p_0 - \log p(z))$ , where the base value of the mixing time scale (where  $p = p_0$ ) within the convectively unstable layer is given by its mixing length theory value  $\tau_{\text{MLT}} = \alpha H_p / v_{\text{conv}}$  and  $\alpha = 2.0$  the mixing length parameter (Ludwig et al. 2002). The slope can be derived from Ludwig (2003) as  $\beta = 2 \sqrt{g_5}$ , where  $g_5$  is the surface gravity in units of  $10^5 \text{ cm s}^{-2}$ . Since the calibration of this relation involved an extrapolation of the M dwarf simulations to lower  $T_{\text{eff}}$ , the models allow for adjusting the slope  $\beta$  by a factor of up to 3, adopting a factor of 1 for the 1800K and 1400K test cases, and 2 for the 600K and 1000K cases.

### 2.2.3 Marley, Ackerman & Lodders model

**2.2.3.1 Dust treatment in model atmosphere code:** The Marley, Ackerman & Lodders - modelling collaboration follows condensable gas as it moves upwards and condenses in the atmosphere of an ultracool dwarf. The composition and cloud structure at each point in a trial atmosphere model is computed, based on the existing profile and then this information is used to iterate towards the next trial profile. The chemistry at each pressure/temperature point is interpolated within a table of atomic and molecular abundances computed for chemical equilibrium (Freedman, Marley & Lodders 2008). The cloud is computed by applying the Ackerman & Marley (2001) cloud model.

**2.2.3.2 Gas-phase treatment:** Abundances of gas species are calculated with the CONDOR code (Lodders & Fegley 1993; Fe-

gley & Lodders 1994; Lodders 2003) which calculates chemical equilibrium compositions by considering the dual constraints of mass balance and chemical equilibrium. Input data required for the code are thermodynamic properties of the gas-phase species and compounds (e.g., equilibrium constants), appropriate elemental abundance tables for the system, temperature and total pressure. The equilibrium constants used in the CONDOR code are computed from the Gibbs free energy ( $\Delta G$ ) data, which are directly proportional to the logarithm of the equilibrium constant ( $\ln K_p$ ) as  $\Delta G = -RT \ln K_p$  ( $T$  – gas temperature,  $R$  – gas constant). The code considers  $\sim 2000$  gas species (including ions) and  $\sim 1700$  solids and liquids for compounds of all naturally occurring elements<sup>4</sup>.

**2.2.3.3 Condensate treatment:** For application to substellar atmospheres, the CONDOR code treats condensate formation by removing primary condensates (i.e., condensates that form from condensing gases) from the gas into cloud layers (Lodders 2004; Lodders & Fegley 2006; see Table 3). An important consequence of this approach is that secondary condensates arising from gas-solid reactions as would be predicted by pure equilibrium are excluded because the primary condensates are assumed to settle into clouds and are thus no longer available for reaction with the cooler gas above the clouds. For example the computation assumes that iron grains (a primary condensate) do not react with  $H_2S$  gas to form FeS at lower temperatures ( $\sim 700$  K) where the secondary FeS would form if Fe metal were still present. Instead the  $H_2S$  remains in the gas phase as is observed in the deep atmosphere of Jupiter (Niemann et al. 1998) where  $H_2S$  is only removed into  $NH_4SH$  clouds below  $\sim 200$  K (Fegley & Lodders 1994; Visscher et al. 2006). Likewise a detection of  $H_2S$  in a cool T dwarf would confirm the inhibition of secondary condensation. Marley et al. (2002) argue that the far red colours of T dwarfs can only be reproduced if secondary condensation of alkali-bearing phases is indeed inhibited.

Both the cloud model of the settling of primary condensates and the chemical equilibrium model assume that at a given temperature below the condensation temperature the gas phase abundances of the elements sequestered by condensation are set by the respective vapour pressure of the primary condensate. With this common assumption the cloud and chemical computations are fully self-consistent.

**2.2.3.4 Cloud model:** The cloud model (Ackerman & Marley 2001) parameterises the efficiency of sedimentation of cloud particles relative to turbulent mixing through a scaling factor,  $f_{sed}$  (Eq. 4 in Ackerman & Marley 2001). Large values of  $f_{sed}$  correspond to rapid particle growth and large mean particle sizes. In this case sedimentation is efficient, which leads to physically and optically thin clouds. When  $f_{sed}$  is small particles are assumed to grow more slowly and the amount of condensed matter in the atmospheric is larger and clouds thicker. In this sense small  $f_{sed}$  is somewhat comparable to the Tsuji models with a large difference between  $T_{cond}$  and  $T_{crit}$  while large  $f_{sed}$  is similar to the opposite case. Unlike the Tsuji models Ackerman & Marley (2001) compute a particle size profile for each condensate in each model atmosphere.

For a fixed atmospheric profile,  $f_{sed}$  and a description of the width of the particle size distribution, the Ackerman & Marley (2001) model uniquely predicts the variation in mean particle size and particle number density through the atmosphere. Thus families

of models, i.e. set of models with varying sets of parameters  $T_{eff}$ ,  $\log g$ ,  $f_{sed}$ , each with a unique  $f_{sed}$ , can be produced. No attempt is made to model microphysical processes of dust growth and coagulation. Instead it is assumed that the micro-physical processes acting within the cloud are able to produce the particle sizes implied by any specified value of  $f_{sed}$ .

In terrestrial rain clouds the particle size distribution is often double-peaked (Ackerman et al. 2001), with small particles that grow from condensation of the vapour co-existing with larger drops that have grown by collisions between particles. In the Ackerman & Marley (2001) approach a single, broad log-normal particle size distribution is intended to capture the likely existence of such a double-peaked size distribution. They employ a width  $\sigma = 2$  for all cases, although this can in principle be varied.

Like the Allard & Homeier - model, the Marley, Ackerman & Lodders cloud - model use the mixing length theory to compute gas velocities in the convection zone and must employ some other description to specify velocities above the radiative-convective boundary. They describe mixing in radiatively stable layers by specifying an eddy diffusion coefficient,  $K_{eddy} = H^2/\tau_{mix}$ , where  $H$  and  $\tau_{mix}$  are the scale height and mixing time. Experience with the radiative stratospheres in the solar system (e.g., Atreya et al. 1991; Bishop et al. 1995; Moses et al. 2004) shows that typical values of  $K_{eddy}$  in these atmospheres lie in the range of  $10^4$  to  $10^7$  cm<sup>2</sup>s. Observations of ammonia and CO in the atmosphere of the T7.5 dwarf Gliese 570D imply  $K_{eddy} \sim 10^6$  cm<sup>2</sup>s (Saumon et al. 2006; Geballe et al. 2008). Comparisons of the mid-infrared colours of L dwarfs to models that include chemical mixing (Leggett et al. 2006), suggest  $K_{eddy} \sim 10^4$  cm<sup>2</sup> s<sup>-1</sup>. The Marley, Ackerman & Lodders - models reported here set  $K_{eddy} \geq 10^5$  cm<sup>2</sup> s<sup>-1</sup> at all points in the atmosphere with a smooth transition from the convective zone to this value.

As with variation of cloud thickness to match variation in  $J-K$  at fixed  $T_{eff}$  in the Tsuji models, changes in  $f_{sed}$  produce atmosphere models with a range of near-infrared spectra and colours. Burgasser et al. (2007) and Stephens et al. (2008) have shown that the spectra of bluer-than-average L dwarfs can be fit by models employing large  $f_{sed}$  while redder-than-average L dwarfs seem to require small  $f_{sed}$ . The Marley, Ackerman & Lodders reproduce spectra across the L to T transition by employing models with progressively larger  $f_{sed}$  with later spectral type (Cushing et al. 2008; Stephens et al. 2008; Leggett et al. 2008).

## 2.2.4 Helling & Woitke model

**2.2.4.1 Dust treatment for a model atmosphere code:** The Helling & Woitke approach is fundamentally different from the previous models in two important ways. First, this model follows the trajectory of an ensemble of dust grains downwards from the top of the atmosphere instead of upwards from the bottom. This approach is based on the phenomenological analogy to thunderstorm where large air masses are advected upwards before raindrops do form. Dust clouds in substellar objects are considered stationary, i.e. uncondensed gas is mixed upward from which dust particles continuously form, settle gravitationally, and evaporate. In this stationary situation, the downward directed element transfer via precipitating dust grains is balanced by an upward mixing from the deep interior by convective and overshoot-motions (Helling et al. 2001b, Helling 2003). The second major difference from the other approach is that the Helling & Woitke approach kinetically describes the cloud particle formation as phase-transition process by modelling seed formation, grain growth/evaporation, sedimentation in phase-non-equilibrium, element depletion, and their in-

<sup>4</sup> All elements up to Bi (number 83) excepting Tc and Pm but adding Th and U, for a total of 83.

teractions. Dust moment equations describing these processes are derived from rate equations and are solved as a function of height  $z$  for a given  $(T, p, v_{\text{conv}})$  atmosphere structure. The equations are integrated inward.

**2.2.4.2 Gas-phase treatment:** The composition of the gas phase is calculated assuming chemical equilibrium for 14 elements (H, He, C, N, O, Si, Mg, Al, Fe, S, Na, K, Ti, Ca) and 158 molecules with equilibrium constants fitted to the thermodynamical molecular data of the electronic version of the JANAF tables (Chase et al. 1986). The equilibrium constant for TiC are from Gauger et al. (see Helling et al. 2000), for CaH from Tsuji (1973), and FeH from Burrows (priv. com.). Solar elemental abundances are assumed at the lower boundary of the model atmosphere, assuming a well-mixed gas-phase solar composition, and first ionisation states of the elements are calculated. Element conservation equations are auxiliary conditions which take into account the loss of elements in the gas phase by nucleation, growth, and drift and the gain by evaporation (Woitke & Helling 2004).

**2.2.4.3 Condensate treatment:** The condensates considered during the solution of the Helling & Woitke dust model equations are treated in full phase-non equilibrium. The supersaturation ratio  $S$  is calculated from the gas phase composition in chemical equilibrium.

**2.2.4.4 Cloud model:** The dust formation starts with the formation of seed particles (nucleation). The nucleation rate is calculated for homogeneous  $(\text{TiO}_2)_N$ -clusters applying the modified classical nucleation theory (Gail et al. 1984; see Eq. 34 in Helling & Woitke 2006). The calculation of the nucleation rate relies on quantum mechanical calculations for the formation of  $\text{TiO}_2$ -seeds by a step-wise addition of  $\text{TiO}_2$  molecules (Jeong et al. 2000). The nucleation rate determines the number of dust particles. These seeds grow to macroscopic sizes by gas-solid surface reactions. Because many compounds can be thermally stable almost simultaneously in substellar atmospheres, the simultaneous growth of 12 solids  $\text{TiO}_2[\text{s}]$ ,  $\text{SiO}[\text{s}]$ ,  $\text{SiO}_2[\text{s}]$ ,  $\text{Fe}[\text{s}]$ ,  $\text{FeO}[\text{s}]$ ,  $\text{Fe}_2\text{O}_3[\text{s}]$ ,  $\text{FeS}[\text{s}]$ ,  $\text{MgO}[\text{s}]$ ,  $\text{MgSiO}_3[\text{s}]$ ,  $\text{Mg}_2\text{SiO}_4[\text{s}]$ ,  $\text{Al}_2\text{O}_3[\text{s}]$  and  $\text{CaTiO}_3[\text{s}]$  by 60 surface reactions onto  $\text{TiO}_2$ -seed particles is modelled (Helling, Woitke & Thi 2008). These *dirty grains* are modelled to be composed of a homogeneous mix of numerous islands of the different, pure condensates (Helling & Woitke 2006). Drift transports existing particles into region where they might continue to grow before they evaporate in the deeper, warmer atmosphere. While reactions on an existing grain surface proceed if the gas is supersaturated ( $S > 1$ ) with respect to this particular reaction (Helling & Woitke 2006), the seed formation can only take place when the gas is highly supersaturated ( $S \gg 1$ ). If the gas is under-saturated ( $S < 1$ ) the solid will evaporate.

The majority of dust grains that build up the cloud layer are found in a subsonic gas for which Knudsen numbers are small (see Woitke & Helling 2003). The respective kinetic description is solved in form of conservation equations which allows a simultaneous treatment of nucleation, growth, evaporation, drift, and element replenishment. The dust formation is modelled by applying conservation equations of dust moments  $L_j = \int V^{j/3} f(V) dV$  with  $f(V)$  the grain size distribution function. Nucleation, growth/evaporation and gravitational settling are source terms of these equations (Woitke & Helling 2003, Helling & Woitke 2006). The solution of the dust moment equations and element conservations determines quantities like grain sizes, grain material composition, total

grain volume, remaining gas-phase element abundances. The element replenishment is treated by introducing a parameterised mixing time scale  $\tau_{\text{mix}}(z)$ . Ludwig et al. (2002, 2006) show that, generally speaking, the convectively excited hydrodynamical motions – and thereby the mixing – decay exponentially with increasing height above the convectively unstable zone resulting in an exponential decrease of the mass exchange frequency in the radiative zone from which  $\tau_{\text{mix}}(z)$  is derived as  $\log \tau_{\text{mix}}(z) = \log \tau_{\text{mix}}^{\text{min}}(z) + \beta \cdot \{0, \log p_0 - \log p(z)\}$  with  $p_0$  the pressure at the upper edge of the convective unstable zone,  $\tau_{\text{mix}}^{\text{min}}(z) = \alpha / H_p v_{\text{conv}}$  ( $\alpha = 2.0$ ) the minimum value of the mixing time-scale occurring in the convectively unstable region and  $\beta = \Delta \log f_{\text{exchange}} / \Delta \log p \approx 2.2$ .

### 2.2.5 Dehn & Hauschildt + Helling & Woitke model

**2.2.5.1 Dust treatment in model atmosphere:** The dust cloud model of Helling & Woitke (Sect. 2.2.4) has been adopted as module in the static PHOENIX model atmosphere code (Dehn 2007; Helling et al. 2008 a,b). the dust module receives the  $(T(z), p(z), v_{\text{conv}}(z))$  structure from PHOENIX and provides the dust number density, the solid's volume fractions, the mean grain size, and the remaining element abundances in the gas phase for each atmospheric layer. Effective medium and Mie theory are then used to calculate the dust opacity in addition to the usual gas-phase opacity calculations. The temperature structure is found iteratively by a modified Unsöld-Lucy correction algorithm. The adjusted atmosphere structure, including the solution of mixing-length theory to find  $v_{\text{conv}}$ , is an input for the dust module in the next iteration. Compared to the classical PHOENIX solution, the computing time has increases by a considerable factor of since for each temperature iteration the dust module is called. The dust module itself iterates to solve the dust moment equation by fulfilling the element conservation auxiliary condition.

**2.2.5.2 Gas-phase treatment, condensate treatment, cloud model:** The gas-phase composition is calculated assuming chemical equilibrium as described in Sect. 2.2.2. The cloud model is a reduced version of Sect. 2.2.4 in order to keep the computation time effortable: The simultaneous growth of 7 solids  $\text{TiO}_2[\text{s}]$ ,  $\text{SiO}_2[\text{s}]$ ,  $\text{Fe}[\text{s}]$ ,  $\text{MgO}[\text{s}]$ ,  $\text{Mg}_2\text{SiO}_3[\text{s}]$ ,  $\text{Mg}_2\text{SiO}_4[\text{s}]$ ,  $\text{Al}_2\text{O}_3[\text{s}]$  onto the  $\text{TiO}_2$ -seed particles is considered. Only 32 surface reaction are taken into account (Dehn 2007).

## 3 TEST CASES

We explored the characteristics and capabilities of the cloud models summarised in Sect. 2 with two sets of test calculations. The **test case 1** is the component-based test study (Kleb & Wood 2004), and it is designed to compare the dust cloud models alone by separating them from hydrodynamics and radiative transfer treatments (including opacity calculations). **Test case 2** utilises the method of manufactured solutions (Kleb & Wood 2004), and compares the results of completely iterated substellar model atmosphere simulations. Table 1 contains the definitions of the quantities discussed in the following.

### 3.1 Test case 1: local quantities given

Each dust cloud model is calculated for a prescribed set of  $(T, p_{\text{gas}}, \epsilon_i^0, v_{\text{conv}})$  or  $(T, p_{\text{gas}}, \epsilon_i^0, F_{\text{conv}})$  profiles with  $T$  the local gas temperature,  $p_{\text{gas}}$  the local gas pressure,  $v_{\text{conv}}$  and  $F_{\text{conv}}$  being the

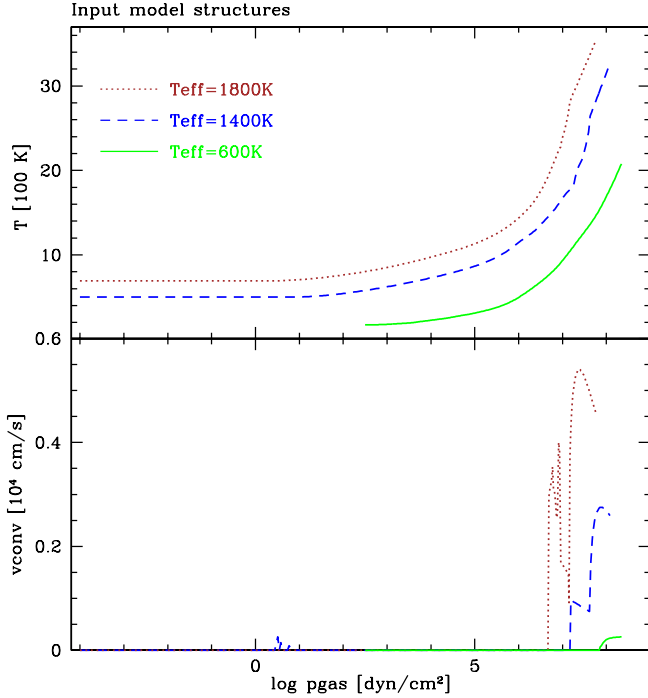


**Figure 1.** Input model structure ( $T, p, v_{\text{conv}}$ ) for  $T_{\text{eff}} = 1800, 1400, 600$  K with  $\log g = 5.0$  and solar element abundances.

convective velocity and the convective flux, respectively (Fig. 1). The deep, well-mixed element abundances  $\epsilon_i^0$  ( $i = \text{H, Si, Mg, Ti, } \dots$ ) in the inner atmosphere have been chosen as solar according to Grevesse, Noels & Sauval (1992).

**REMARKS ON THE SOLAR ELEMENT ABUNDANCES:** The solar element abundances published by Anders & Grevesse (1989), Grevesse, Noels & Sauval (1992), and Grevesse & Sauval (1998) are undergoing considerable revisions but an agreement on the most correct value according to present knowledge has not yet been reached. The oxygen element abundance, as the most prominent example, has been revised downward to  $\epsilon_o^0 = 8.66 \pm 0.05$  by Asplund et al (2004) and to only  $\epsilon_o^0 = 8.76 \pm 0.07$  by Caffau et al (2008), both based on 3D hydrodynamical simulations of the solar photosphere in combination with non-LTE line transfer (see discussion in Caffau et al. 2008). However, Ayres et al. (2006) suggest  $\epsilon_o^0 = 8.84$  from their measured solar CO lines. Additionally, the downward revision of the oxygen abundances greatly increases the difference between the internal sound speed predicted by solar models and the sound speed inferred from helioseismology (Christensen-Dalsgaard et al. 2008). The determination of solar element abundances is a fundamental problem for atmosphere physics and chemistry, and the final amount of dust formed in a cloud will depend on the element abundance values. However, the test of its implications goes beyond the scope of this paper. Therefore, **test case 1** (Sect. 3.2) applies the Grevesse, Noels & Sauval (1992). The element abundances used for **test case 2** (Sect. 3.4) are listed in Table 5 for each of the atmosphere codes.

**REMARKS ON THE MIXING TIME-SCALE  $\tau_{\text{mix}}$ :** A mixing time-scale  $\tau_{\text{mix}}$  enters all cloud models except the Tsuji-model. Each model (Marley, Ackerman & Lodders, Allard & Homeier, Helling & Woitke) does interpret, and hence, uses  $\tau_{\text{mix}}$  in different ways. In the Marley, Ackerman & Lodders-model, the sedimentation efficiency is parameterised relative to a mixing time-scale through a scaling fac-

tor  $f_{\text{sed}}$ , the Allard & Homeier-model includes a  $\tau_{\text{mix}}$  in a time-scale comparison to determine local mean grain sizes, and a  $\tau_{\text{mix}}$  influences the rate of seed formation, the growth and the settling process since it enters a set of conservation equations in the Helling & Woitke-model. Hence, we refrain from directly comparing the mixing time-scales of the different cloud models, since a comparison of  $\tau_{\text{mix}}$  would be rather misleading regarding the cloud properties derived by each of the modeller groups.

We have chosen to compare the models for the following stellar parameter which can be considered as examples for the L-, L-T, and T-dwarf atmospheres:

L – dwarf	$T_{\text{eff}} = 1800\text{K}$ (provided by M. Dehn)
L – T dwarf	$T_{\text{eff}} = 1400\text{K}$ (provided by M. Dehn)
T – dwarf	$T_{\text{eff}} = 600\text{K}$ (provided by M. Marley)

All models have  $\log g = 5.0$ . The given ( $T, p$ ) and ( $v_{\text{conv}}, p$ ) structures are shown in Fig. 1. The  $T_{\text{eff}} = 600\text{K}$  model is considerably less extended in  $\log p$  than the hotter models. Its convective velocity is very small. Therefore, a much less efficient convective overshooting is anticipated, and (for those models which assume gaseous transport) a less efficient element replenishment of the upper atmospheric layers.

### 3.2 Results: test case 1

We compare four essential results of our dust cloud models which are needed for the opacity calculations in a complete atmosphere model:

- *dust content*
- *mean particle size*
- *dust material composition*
- *gas-phase composition*

#### 3.2.1 Dust content in the atmosphere

We measure the dust content in the atmosphere by the dust-to-gas mass ratio  $\rho_{\text{dust}}/\rho_{\text{gas}}$  (for definition see Table 1; Fig. 2 left). However, the phase-equilibrium models allow two interpretation of this quantity, namely, the amount of dust acting as opacity source and the amount of dust acting as element sink (compare column 6 in Table 5). Figure 2 depicts  $\rho_{\text{dust}}/\rho_{\text{gas}}$  for dust opacity sources, and demonstrate for the Allard & Homeier-model that the difference to  $\rho_{\text{dust}}/\rho_{\text{gas}}$  for dust element sinks can be significant.

The dust-to-gas mass ratio shows where most of the dust is located in the cloud layers, and the extension of the cloud layer(s) differs for all models. The innermost cloud layers generally contain the maximum amount of dust, except in the Tsuji results where the clouds extension varies with  $T_{\text{cr}}$ . All models have the same location of the inner boundary of the cloud (*cloud base*), since it is determined mainly by thermal stability.

The maximum  $\rho_{\text{dust}}/\rho_{\text{gas}}$  is of about the same order of magnitude for all models but the exact values differ (see Table 4). Note that the amount of dust entering the radiative transfer calculation is usually smaller than the amount of dust causing the gas phase depletion in phase-equilibrium models (compare Allard & Homeier-model: gray lines in Fig. 2, left). The maximum  $\rho_{\text{dust}}/\rho_{\text{gas}}$  value is reached at different atmospheric altitudes in the different models and it retains its value over different atmospheric extension. The Tsuji-models suggest the highest amount of dust in the atmospheres for  $T_{\text{cr}} = 1700\text{K}$ . The Allard & Homeier-models suggest the lowest amount of dust. The  $T_{\text{eff}} = 600\text{K}$  test case is challenging



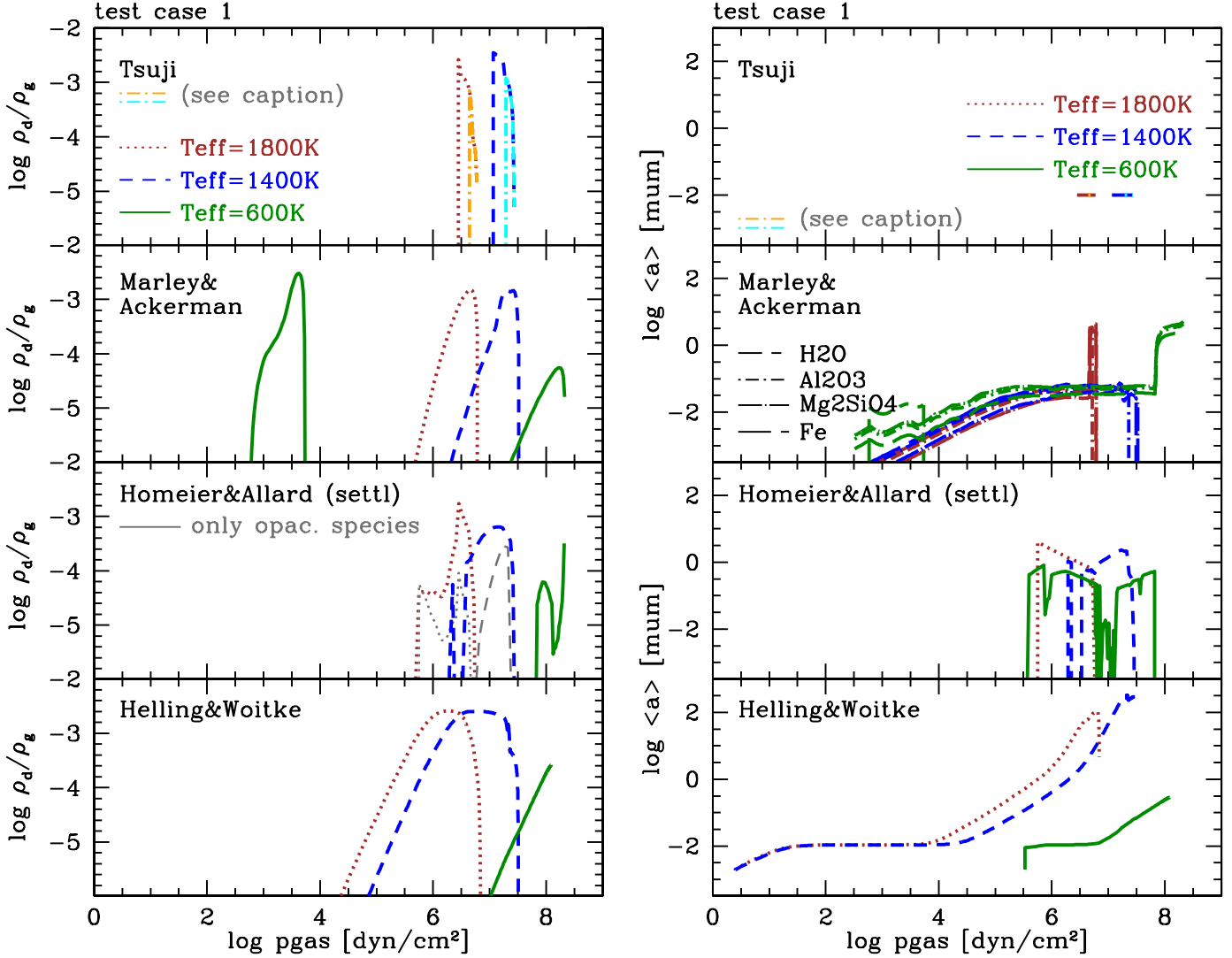


**Figure 2.** Test case 1 results for prescribed atmospheric structures for  $T_{\text{eff}}=1800, 1400, 600\text{K}$ , all  $\log g = 5.0$  and solar element abundance. **Left:** Dust-gas-ratio  $\rho_d/\rho_g$  **Right:** Mean particle size  $\langle a \rangle$  [μm]

**Note:** For Tsuji two cases of  $T_{\text{cr}}$  are plotted for each  $T_{\text{eff}}$ :  $T_{\text{cr}} = 1900\text{K}$  – light colours (orange/light blue),  $T_{\text{cr}} = 1700\text{K}$  – dark colours (red/blue). For Marley, Ackerman & Lodders  $\rho_d/\rho_g = (\rho_{\text{Al}_2\text{O}_3} + \rho_{\text{Fe}} + \rho_{\text{Mg}_2\text{SiO}_4} + \rho_{\text{H}_2\text{O}})/\rho_g$  ( $f_{\text{sed}} = 2$ ). The homogeneous H<sub>2</sub>O-, Al<sub>2</sub>O<sub>3</sub>-, Mg<sub>2</sub>SiO<sub>4</sub>-, and Fe-particle have different sizes (different line styles). For Allard & Homeier  $\rho_d/\rho_g$  includes all species contributing to the depletion of the gas phase. The gray lines show their values which enters the radiative transfer calculation. For the Allard & Homeier  $T_{\text{eff}} = 600\text{K}$ -model, the opacity-species-only- $\log \rho_d/\rho_g$  values fall below the axis range depicted. For Helling & Woitke, the code has difficulties calculating clouds for  $T_{\text{eff}} = 600\text{K}$  in the inner atmosphere.

for all models: No data could be provided from the Tsuji-model, the Allard & Homeier  $\rho_{\text{dust}}/\rho_{\text{gas}}$  have a local minimum, and the Helling & Woitke-model reaches the shallowest depth. The Marley, Ackerman & Lodders  $T_{\text{eff}} = 600\text{K}$ -model (solid green line in Fig. 2) shows two well-separated cloud layers: a water layer high up in the atmosphere at  $\approx 10$  dyn/cm<sup>2</sup> and a silicate layer between  $10^7 \dots 10^8$  dyn/cm<sup>2</sup> (compare Sect. 3.2.3). All other models produce only the silicate layer.

### 3.2.2 Mean particles sizes in the cloud layer

Figure 2 (right) shows the results for the means grain sizes  $\langle a \rangle$  (definition see Table 1) calculated for given  $(T, p, v_{\text{conv}})$  profiles. The mean grain sizes are different amongst all models which reflects the different model assumptions made. Also, the grain size distri-

bution function  $f(a)$  used to determine  $\langle a \rangle$  is different in each of the dust cloud models (see Table 2).

A common feature for all models is that small mean particle sizes  $\langle a \rangle \lesssim 10^{-2}\mu\text{m}$  populate the upper cloud regions, except in the Allard & Homeier-model. This small grain size in the upper cloud layers are associated with very small dust-to-gas ratios of  $\rho_{\text{dust}}/\rho_{\text{gas}} < 10^{-6}$ . Particle sizes increase inward and reach a certain maximum size (Marley, Ackerman & Lodders; Helling & Woitke), or are constant by assumption in the entire cloud (Tsuji), or they reflect a complicated time-scale competition (Allard & Homeier). The grains of different kind  $s$  have different distributions  $f_s(a, z)$  in Marley, Ackerman & Lodders-model (i.e. Fe[s]-grains, H<sub>2</sub>O[s] grains – different line styles in Fig. 2, 3<sup>rd</sup> panel). Grains of different but homogeneous composition have the same size distribution in the Allard & Homeier and in the Tsuji-models at a particular height in the atmosphere. The dirty grains (i.e. a mixture of Fe[s]-SiO[s]-

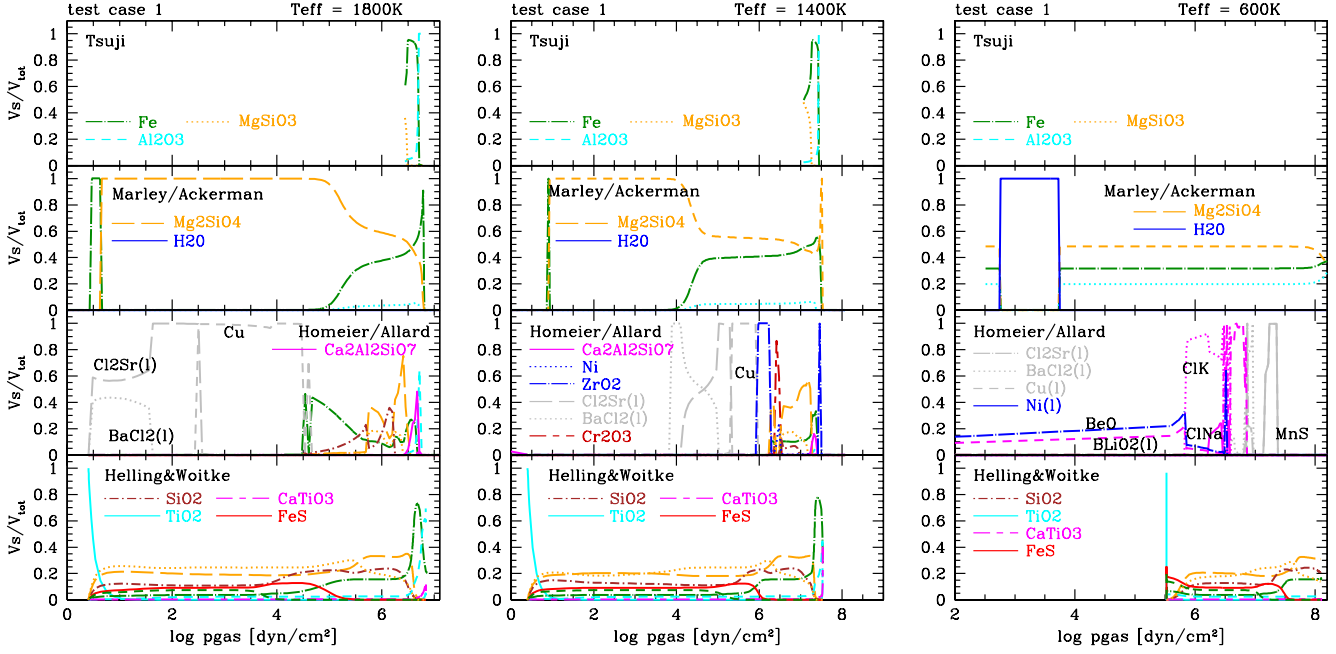


**Figure 3.** Cloud material composition in volume fractions of total dust volume  $V_s/V_{\text{tot}}$  for prescribed model atmospheres of  $T_{\text{eff}}=1800, 1400, 600\text{K}$ ,  $\log g = 5.0$  (Tsuji:  $T_{\text{cr}} = 1700\text{K}$ , Marley, Ackerman & Lodders:  $f_{\text{sed}} = 2$ ) resulting from different dust cloud models.

**Note:** For Allard & Homeier  $V_{\text{Al}_2\text{O}_3}/V_{\text{tot}} = (V_{\text{Al}_2\text{O}_3-\text{c}1} + V_{\text{Al}_2\text{O}_3-\text{c}2} + V_{\text{Al}_2\text{O}_3-\text{c}3})/V_{\text{tot}}$  and  $V_{\text{Fe}}/V_{\text{tot}} = (V_{\text{Fe}-\text{c}} + V_{\text{Fe}-\text{c}1})/V_{\text{tot}}$  with c, c1, c2, c3 being different crystal structures treated in their equilibrium ansatz. For Tsuji no  $T_{\text{eff}} = 600\text{K}$  model is available.

**Table 4.** Maximum dust-to-gas ratios  $\log(\rho_{\text{dust}}/\rho_{\text{gas}})_{\text{max}}$ , the maximum mean grain sizes  $\log \langle a \rangle$  [ $\mu\text{m}$ ] and its value in the upper cloud layers @  $10^3 \text{ dyn/cm}^2$  in different dust models for given  $(T, p_{\text{gas}}, v_{\text{conv}})$  profiles.

	$T_{\text{eff}}$	Tsuji	Marley, Ackerman & Lodders	Allard & Homeier	Helling & Woitke
dust content	1800K	-3.6	-3.2	-3.2	-3.4
$\log \rho_{\text{dust}}/\rho_{\text{gas}}$	1400K	-3.6	-3.2	-2.8	-3.4
	600K		-5.8 (silicates) -3.5 ( $\text{H}_2\text{O}$ )	-4.5	-4.4
grain size	1800K	-2	-1.4 ... -1.6	0	-2
$\log \langle a \rangle$ @	1400K	-2	-1.4 ... -1.6	0	-2
$10^3 \text{ dyn/cm}^2$	600K		-1.6 ... -2	0	0
maximum	1800K	-2	+0.5	+0.7	+2.0
grain size	1400K	-2	1	+0.5	+2.5
$\log \langle a \rangle_{\text{max}}$	600K	-2	+0.5	1	-0.5

$\text{Mg}_2\text{SiO}_4[\text{s}]$  etc.) in the Helling & Woitke-model are characterised by one mean grain size distribution  $f(a, z)$  at a particular height  $z$  in the atmosphere. The transition from  $\langle a \rangle_{\text{min}}$  to  $\langle a \rangle_{\text{max}}$  across the cloud layer appears smoothly in the Helling & Woitke models. The Marley, Ackerman & Lodders- models reach their  $\langle a \rangle_{\text{max}}$  abruptly at about the same latitude. Also the Allard & Homeier models show a sudden rise in mean grain size but at a different atmospheric height. Another direct consequence of the different dust cloud modelling is that the values of  $\langle a \rangle_{\text{max}}$  can differ by a factor of 100 (see also Table 4).

### 3.2.3 Dust material composition

The chemical composition of the cloud particles shows the largest variation between the different models. Figure 3 shows the material

composition of the test models  $T_{\text{eff}} = 1800, 1400, 600 \text{ K}$  in volume fractions of the total dust volume,  $V_s/V_{\text{tot}}$  (definition  $\nearrow$  Table 1), for the different cloud models. We only consider dust species which are important for the gas and dust opacity in the radiative transfer calculations in Sect. 3.3 ( $\nearrow$  Table 5). The calculation of the dust composition varies widely in the different models and splits into two classes: dust particles of homogeneous composition assuming equilibrium condensation (Tsuji; Marley, Ackerman & Lodders; Allard & Homeier) and dirty dust particles of heterogeneous composition according to the kinetic treatment of growth and evaporation (Helling & Woitke). The chemical heterogeneity of the whole dust complex in the equilibrium models is reached by considering ensembles of pure  $\text{Fe}[\text{s}]$ -grains,  $\text{Al}_2\text{O}_3[\text{s}]$ -grains etc.

The Tsuji and the Marley, Ackerman & Ackerman-models allow for the 3 and 5 major condensates, respectively, as dust opacity sources. The dominating low-temperature condensate is  $\text{Mg}_2\text{SiO}_3[\text{s}]$  in the Tsuji-model and  $\text{Mg}_2\text{SiO}_4[\text{s}]$  in the Marley, Ackerman & Lodders-model. The  $\text{Fe}[\text{s}]$  fraction increases with decreasing  $T_{\text{eff}}$  in both models at intermediate temperatures. Also in the Helling & Woitke-model  $\text{Mg}_2\text{SiO}_3[\text{s}]$  and  $\text{Mg}_2\text{SiO}_4[\text{s}]$  are the dominant low temperature condensates in addition to  $\text{SiO}_2[\text{s}]$  and  $\text{FeS}[\text{s}]$ . Note that  $\text{SiO}_2[\text{s}]$  is never predicted by the equilibrium models. The  $\text{Fe}[\text{s}]$  content increases inward until it reaches, like in the other models, a pronounced maximum near the inner cloud edge. The dust at the cloud base is made of  $\text{Al}_2\text{O}_3[\text{s}]$  with possible impurities of  $\text{CaTiO}_3[\text{s}]$  ( $T_{\text{eff}}=1800, 1400\text{K}$ ) in the Helling & Woitke-model. The most refractory cloud condensate layer in Marley, Ackerman & Lodders-models is composed of corundum or Ca-Aluminates which serve as element sinks, hence, not depicted in Fig. 3. The Allard & Homeier-models only partially agree with these results. The Marley, Ackerman & Lodders-model is the only model which includes  $\text{H}_2\text{O}[\text{s}]$  as possible condensate which

allows for a second, detached cloud layer above the already discussed oxide-silicate cloud layer (compare Fig. 2).

Given the great diversity in grain composition with different model assumptions, we must conclude that the chemical composition of the cloud particles in substellar atmospheres is still uncertain.

### 3.2.4 Gas-phase chemistry results

Figure 4 shows the number densities  $n$  [ $\text{cm}^{-3}$ ] for a selected number of gas phase Si-, Mg-, Al-, Ca-, and Ti-bearing molecules. We additionally plot the most important H-molecules and the most important C-bearing molecules (7<sup>th</sup> and 8<sup>th</sup> panel). All models assume the gas-phase to be in chemical equilibrium ( $\nearrow$  Sect. 2.1). All models used the same well-mixed element abundances  $\epsilon_i^0$  at the inner boundary of the cloud mode ( $\nearrow$  Sect. 3.1). Hence, different gas-phase number densities produced by the models are a consequence of the different treatment of dust formation which leads to different remaining element abundances  $\epsilon_i$  in the gas phase. The comparison of the remaining gas phase (after cloud formation) is needed to understand possible spectral trends in the later test cases of the complete (sub-)stellar atmosphere model (Sect. 3.3).

**3.2.4.1  $\text{H}_2$ ,  $\text{H}_2\text{O}$ ,  $\text{NH}_3$ :** The first test for differences in the chemical equilibrium gas-phase composition considers  $\text{H}_2$ . Because of the continuous community interest we include  $\text{H}_2\text{O}$ , and  $\text{NH}_3$  for its increasing spectral importance with decreasing  $T_{\text{eff}}$  in the sub-stellar regime. The  $\text{H}_2$  and  $\text{H}_2\text{O}$  abundances are almost identical for all models. Figure 4 shows agreement also for the  $\text{NH}_3$  abundances except for the Allard & Homeier-model which predicts an overabundance of  $\text{NH}_3$  compared to the other models.

**3.2.4.2  $\text{CO}$ ,  $\text{CH}_4$ :** These molecules are only little effected by dust formation, since carbon solids are not considered in the models under investigation. Hence, they are a good test for the general agreement of the gas-phase composition with respect to element abundances and material constants. However, the consumption of oxygen by the silicates and oxides does also affect the amount of gas-phase  $\text{CO}$ , hence indirectly also  $\text{CH}_4$ , due to oxygen depletion. We observe that all models predict  $\text{CH}_4$  to be the major C-bearing molecule above a certain height in the atmosphere below which  $\text{CO}$  takes over. Beside this general agreement amongst the models, the  $\text{CO}$  number densities differ above the cloud layer, most likely resulting from different equilibrium constants for  $\text{CO}$  and  $\text{CH}_4$ .

**3.2.4.3  $\text{TiO}$ ,  $\text{TiO}_2$ :**  $\text{TiO}_2$  is more abundant than  $\text{TiO}$  in all models though the relative difference varies amongst the models. The models do not agree on the values of the  $\text{TiO}$  and  $\text{TiO}_2$  abundances. The Helling & Woitke model suggests the highest abundances for both molecules, the Tsuji-model suggests the lowest abundances.

**3.2.4.4  $\text{SiO}$ ,  $\text{SiO}_2$ :**  $\text{SiO}$  is more abundant than  $\text{SiO}_2$  in all models though the relative difference varies widely amongst the models. All models agree well for  $p > 10^7 \text{ dyn cm}^{-2}$  which coincides with the pressure-level of the maximum dust content in this model (compare Fig. 2, left). The Tsuji-model again suggest the lowest molecular abundances, and the Helling & Woitke model suggest the highest abundances at lower pressures.

**3.2.4.5  $\text{MgH}$ ,  $\text{MgOH}$ :**  $\text{MgOH}$  is more abundant than  $\text{MgH}$  in all models and the number densities agree well in the inner atmosphere for  $p > 10^7 \text{ dyn cm}^{-2}$ . The molecular abundances of  $\text{MgH}$

and  $\text{MgOH}$  fall into two groups with respect to the upper atmosphere: The Tsuji- and Helling & Woitke-models suggest a high number density. The Allard & Homeier- and Marley, Ackerman & Lodders-model predict the lowest abundances.

**3.2.4.6  $\text{Fe}$ ,  $\text{FeH}$ ;  $\text{AlH}$ ,  $\text{AlOH}$ :** All models suggest that atomic Fe is more abundant than molecular  $\text{FeH}$ , and  $\text{AlOH}$  than  $\text{AlH}$  throughout the atmosphere and agree very well in the inner atmosphere  $p > 10^7 \text{ dyn cm}^{-2}$ . All phase-equilibrium models yield very good agreements for all four molecules, and the Helling & Woitke suggests the highest Fe,  $\text{FeH}$ ,  $\text{AlH}$ , and  $\text{AlOH}$  gas-phase abundances in the outer atmosphere layers.

**3.2.4.7  $\text{CaH}$ ,  $\text{CaO}$ ,  $\text{Ca(OH)}_2$ :** All models suggest that  $\text{Ca(OH)}_2$  is more abundant than  $\text{CaH}$  for  $p < 10^6 \text{ dyn cm}^{-2}$ .  $\text{CaO}$  has generally a much lower abundance than these two molecules. The Helling & Woitke-model produces exceptionally high abundances of the Ca-molecules as result of the limited number of Ca-bearing solids ( $\nearrow$  Sect. 2.2.4). The Tsuji-model suggest the next highest abundances for these molecules.

**3.2.4.8 General:** The general trend is that the phase-equilibrium models (Tsuji, Allard & Homeier, Marley, Ackerman & Lodders) produce lower gas-phase abundances of molecules containing dust-forming elements than the kinetic model (Helling & Woitke) in the upper atmosphere. However, the molecules that are not affected by the chemistry of dust formation (like  $\text{CO}$ ,  $\text{CH}_4$ ,  $\text{H}_2\text{O}$ ) have very similar abundances in the different models. However, differences for these molecules are indicative of the different oxygen-consumption caused by the differences in the dust cloud models, and of possible differences in the material quantities ( $\nearrow$  Sect. 2.1). Those molecules containing rare element (like Al, Ti, Ca) are predicted with very similar abundances in all phase-equilibrium models. Remaining deviations for these molecules are likely due to a missing solid as element sink ( $\nearrow$  Ca Fig. 4). The strongest deviations amongst these models occurs for molecules containing very abundant elements (Si, Mg). Since a large fraction of the Mg- and Si-bearing molecules contributes to the dust formation, the differences in the dust models are imprinted in the remaining gas-phase abundances the strongest. All models agree on the gas-phase composition below the cloud base (vertical black line, Fig. 2, left).

## 3.3 Test case 2: global quantities given

Two sets of stellar parameters were prescribed,

T – dwarf	$T_{\text{eff}}=1000\text{K}$ , $\log g = 5.0$
L – dwarf	$T_{\text{eff}}=1800\text{K}$ , $\log g = 5.0$ ,

for which complete model atmospheres were calculated including the solution of the radiative transfer. All models assume hydrostatic equilibrium, gas-phase chemical equilibrium, and use mixing length theory for treating the convective energy transport. The dust cloud models are those described in Sect. 2, and all cloud approaches assume spherical symmetric cloud particles. Table 5 summarised further details on the atmosphere codes. The cloud modules are the model atmosphere component which is most different amongst the codes under consideration in this paper.

## 3.4 Results test case 2

We compare results for complete stellar atmosphere simulations regarding the

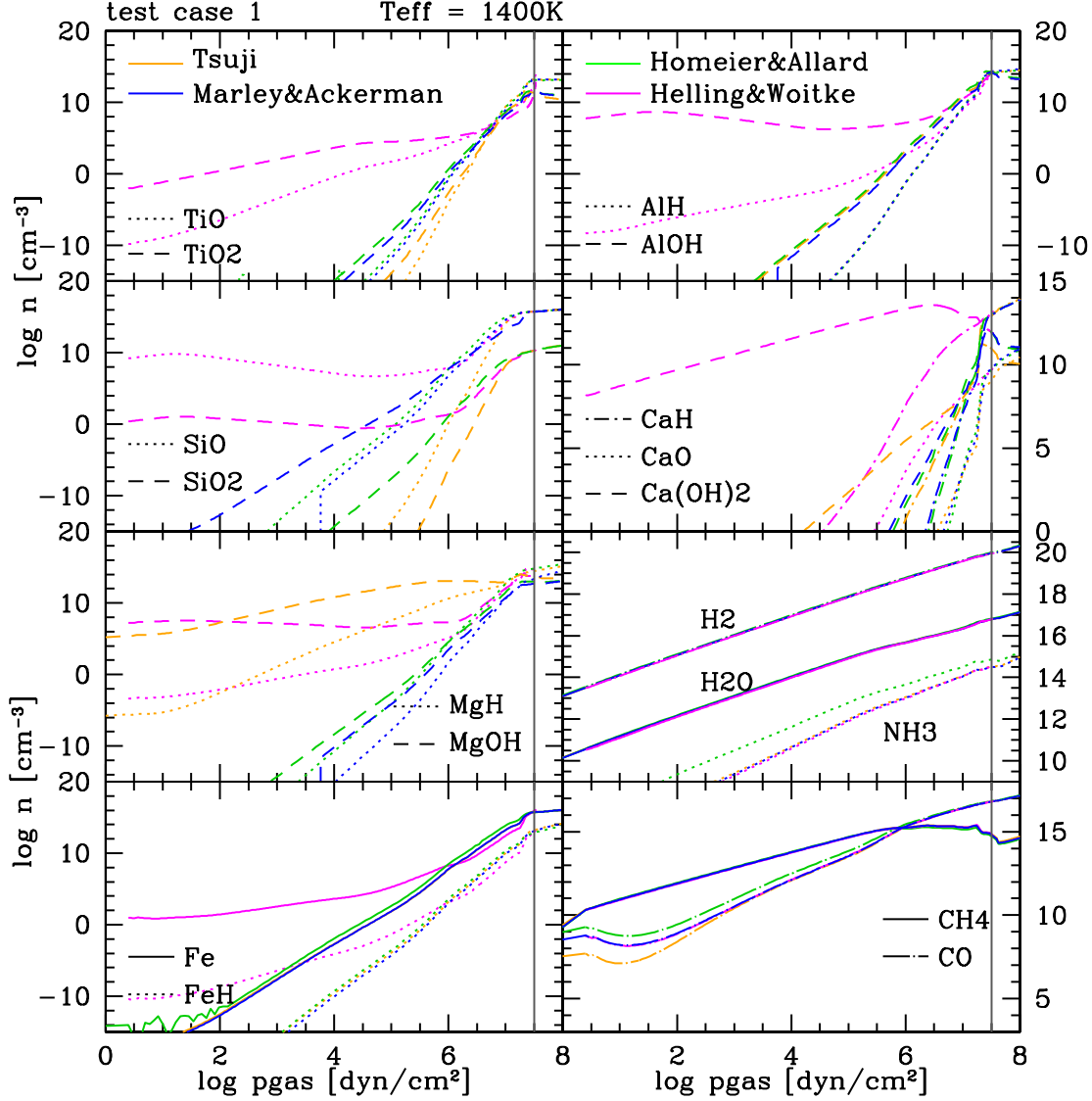


**Figure 4.** Gas phase composition in a cloud forming atmosphere with  $T_{\text{eff}}=1400\text{K}$ ,  $\log g=5.0$  (Tsuji:  $T_{\text{cr}} = 1700\text{K}$ , Marley, Ackerman & Lodders:  $f_{\text{sed}} = 2$ ) as resulting from different cloud model approaches. The vertical thin black line indicates the pressure at the cloud base where  $\rho_d/\rho_{\text{gas}} \rightarrow 0$  ( $\nearrow$  Fig. 2, left).

- atmosphere structure and cloud profile
- spectral energy distribution
- photometric fluxes and colours

### 3.4.1 Atmosphere structure and cloud profiles

Figure 5 shows the  $(T, p, v_{\text{conv}})$ -profiles and the cloud structures of the complete sub-stellar atmosphere simulations.

The  $(T, p)$ -profiles (1<sup>st</sup> panel) differ considerably in all parts of the atmosphere. Note that the Tsuji-model without dust opacity and the Tsuji-model with the highest  $T_{\text{cr}} = 1900\text{K}$  are almost identical. The Dehn & Hauschildt + Helling & Woitke-model is the hottest throughout the entire atmosphere, where the Tsuji- $T_{\text{cr}}=1900\text{K}$ , and the Tsuji-model without dust opacity, as well as the Allard & Homeier-model are the coolest at pressures below  $10^6 \text{ dyn cm}^{-2}$ . All models show the backwarming effect at  $T \approx 2000\text{K}$  for  $T_{\text{eff}} = 1800\text{K}$  except the Allard & Homeier-model, the Tsuji- $T_{\text{cr}}=1900\text{K}$  model, and the Tsuji-model without dust opacity. This backwarming is clearly as-

sociated with occurrence of the cloud layer. It becomes stronger if the maximum amount of dust is situated at higher altitudes as the comparison of the different  $T_{\text{cr}}$ -Tsuji-models demonstrates. The difference to the Allard & Homeier-model is understood by noticing that their model produces much less dust in the respective pressure regime where  $\langle a \rangle \rightarrow 0$  (3<sup>rd</sup> and 4<sup>th</sup> row in Fig. 5; also Fig. 2)

The convective velocity  $v_{\text{conv}}$  explicitly enters all cloud model but the Tsuji-model (2<sup>nd</sup> panel). The Allard & Homeier and the Dehn & Hauschildt + Helling & Woitke-model have identical  $v_{\text{conv}}$  since they use identical modules for treating the convective unstable region below the Schwarzschild limit but differ in the treatment of overshooting into the (classically) convective stable atmosphere at higher altitudes. The Tsuji-model and the Marley, Ackerman & Lodders-model are comparable in  $v_{\text{conv}}$  for the L-dwarf case  $T_{\text{eff}} = 1800\text{K}$ . Both suggest for the T-dwarf models a second convective layer which coincides with maximum  $\rho_{\text{dust}}/\rho_{\text{gas}}$  in these models (Fig. 5, right).

The dust cloud structures are comparable in the sense that

**Table 5.** Summary of the model atmosphere codes used in Sect. 3.3 (s – solids only, sl – liquids and solids)

authors	code name	element abundances	number of elements	number of gas-phase spec.	number of dust species	
<b>Tsuji</b>		Andersen & Grevesse (1989)	34	83	3 as opacity source	s
		Allende Prieto et al.(2002)			10 as element sinks	s
<b>Allard &amp; Homeier</b>	SETTL- PHOENIX	Grevesse, Noels & Sauval (1992)	84	680	43 as opacity source	sl
		Asplund, Grevesse & Sauval (2005)			169 as element sinks	sl
<b>Marley, Ackerman &amp; Lodders</b>		Lodders (2003)	83	~ 2200	5 as opacity source	s
					~ 1700 as element sinks	sl
<b>Dehn &amp; Hauschildt + Helling &amp; Woitke</b>	DRIFT- PHOENIX	Grevesse, Noels & Sauval (1992)	40	338	7 as opacity source	s
					7 as element sinks	s

they appear in approximately the same pressure range except in the Tsuji-model where the small particles are homogeneously distributed in the cloud until a certain critical temperature level  $T_{\text{crit}}$  is reached. All models produce only the cloud layer of silicates and oxides<sup>5</sup> ( $\nearrow$  Sect. 3.2.1). The results differ largely in the details which confirms our results from the first part of our test cases (Sect. 3.2). Different vertical cloud extension are suggested by different simulations: the Allard & Homeier-model produces a vertically less extended cloud layer than the Marley, Ackerman & Lodders-model and the Dehn & Hauschildt + Helling & Woitke - model, which will have consequence for the emergent spectrum of such an atmosphere. It appears that the differences in the cloud properties are amplified if the entire atmosphere problem is taken into consideration. The dust-to-gas ratio  $\rho_{\text{dust}}/\rho_{\text{gas}}$  (3<sup>rd</sup> row in Fig. 5) differs by 2 orders of magnitudes with the dust-opacity free Tsuji-model providing the upper limit and the Dehn & Hauschildt + Helling & Woitke-model, the Allard & Homeier and the Tsuji $_{T_{\text{cr}}=1700\text{K}}$  - models the lower limit. Comparing this with the  $(T, p)$ -profiles (1<sup>st</sup> row) suggests that the higher the local temperatures at a certain pressure level for a given  $T_{\text{eff}}=1800\text{K}$ , the smaller  $\rho_{\text{dust}}/\rho_{\text{gas}}$ :  $(\rho_{\text{dust}}/\rho_{\text{gas}})_{\text{Tsuji}_{T_{\text{cr}}}} > (\rho_{\text{dust}}/\rho_{\text{gas}})_{\text{Marley,Ackerman\&Lodders}} > (\rho_{\text{dust}}/\rho_{\text{gas}})_{\text{Dehn\&Hauschildt+Helling\&Woitke}}$ . This trend re-appears for  $T_{\text{eff}}=1000\text{K}$  for which no Dehn & Hauschildt + Helling & Woitke-model is available. The Allard & Homeier-models are amongst the coolest of the  $(T, p)$ -profiles for a given  $T_{\text{eff}}$  but always suggest a smaller  $\rho_{\text{dust}}/\rho_{\text{gas}}$ .

No trend appears in the numerical data for the mean particle sizes  $\langle a \rangle$ . The models suggest the biggest particles to appear at the cloud base except the Tsuji-model which assumes a constant size in the entire cloud. Note that the particle sizes in the Allard & Homeier-models show a very steep distribution towards the maximum size at the cloud base. It is apparent from Fig. 5 that the different dust cloud treatments produce different grain size distributions in the atmosphere resulting in differences in grain sizes up to 2 orders of magnitude at the cloud top where detectable spectral features would be produced (compare Marley, Ackerman & Lodders and Dehn & Hauschildt + Helling & Woitke). The Allard & Homeier-models suggest no particles in these cloud layers, hence, spectral dust features in these models might be more easily masked by molecular bands.

### 3.4.2 Spectral energy distribution

The spectral energy distributions (SEDs) between  $0.5 \dots 18\mu\text{m}$  calculated by the different model atmosphere codes employing different cloud models are depicted in Fig. 6 ( $T_{\text{eff}} = 1800\text{K}$ ) and Fig. 7 ( $T_{\text{eff}} = 1000\text{K}$ ). The Marley, Ackerman & Lodders model for  $T_{\text{eff}} = 1000\text{K}$  employed  $f_{\text{sed}} = 2$  for consistency with the  $T_{\text{eff}} = 1800\text{K}$  case. Modeling by this group suggests that the spectra of early T dwarfs are better fit with larger values of  $f_{\text{sed}}$ . The thick clouds resulting from the choice of  $f_{\text{sed}} = 2$  (Fig. 5, bottom right) are responsible for the shallow absorption bands and red colors compared to the other groups for this case. In the Tsuji-case we plot two models,  $T_{\text{cr}} = 1700\text{K}$  and  $T_{\text{cr}} = 1900\text{K}$  which demonstrate a very thin ( $T_{\text{cr}} = 1900\text{K}$ ) and an extended ( $T_{\text{cr}} = 1700\text{K}$ ) cloud layer. No two codes produce identical SEDs. Generally, Allard & Homeier and the Tsuji $_{T_{\text{cr}}=1900\text{K}}$ -models appear brighter than the other models between  $\sim 0.8 \dots \sim 1.5\mu\text{m}$  in the optical and near-IR (see also left panels Fig. 8). The Dehn & Hauschildt + Helling & Woitke, the Marley, Ackerman & Lodders and the Tsuji $_{T_{\text{cr}}=1700\text{K}}$ -models are the brightest of all models  $T_{\text{eff}}=1800\text{K}$  in the IR for  $\lambda > 5\mu\text{m}$ . This result is not surprising because the Dehn & Hauschildt + Helling & Woitke, the Marley, Ackerman & Lodders and the Tsuji $_{T_{\text{cr}}=1700\text{K}}$ -models contain the highest amount of small dust particles in the upper cloud layers (Sect. 3.4.1) and should therefore produce a redder atmosphere compared to a model without dust at comparable atmosphere pressures. In principle, the same analysis applies for the  $T_{\text{eff}} = 1000\text{K}$ -case, representing the T-dwarf regime within this study (Fig. 7). The cloud has moved already considerably below  $\tau = 1$  that both Tsuji-models appear very similar. Additionally, the Allard & Homeier-model suggests more spectral flux in several wavelength intervals than the Tsuji $_{T_{\text{cr}}=1900\text{K}}$ -model with an extended cloud layer. Figure 7 also demonstrates an appreciable difference of the Tsuji-models around  $10\mu\text{m}$  which are sensitive to the application of the JOLA opacity band model.

It is apparent from Fig. 8 that the Tsuji $_{T_{\text{cr}}=1900\text{K}}$ , the Marley, Ackerman & Lodders-models and the Dehn & Hauschildt + Helling & Woitke-model produce much shallower absorption features in particular in the optical and near-IR than the Tsuji $_{T_{\text{cr}}=1700\text{K}}$  and the Allard & Homeier-models. Again, the reason lies in the differences in cloud modelling. This result appears surprising for the Dehn & Hauschildt + Helling & Woitke model since more elements remain in the gas phase due to incomplete dust formation, hence, the absorption features should be deeper. A comparison with Fig. 5 (top panel) resolves this: All models showing shallow absorption features are amongst the hottest  $(T, p)$  structures, hence, have low densities at given atmospheric temperature and therefore lower opacity at that atmospheric height. Note that the  $(T, p)$ -

<sup>5</sup> The term *silicate* is loosely used among astronomers. In accordance with mineralogy, silicates are those solids containing Si–O groups. All other solids, like  $\text{Al}_2\text{O}_3[\text{s}]$ ,  $\text{TiO}_2[\text{s}]$ ,  $\text{CaTiO}_3[\text{s}]$  etc. are oxides.

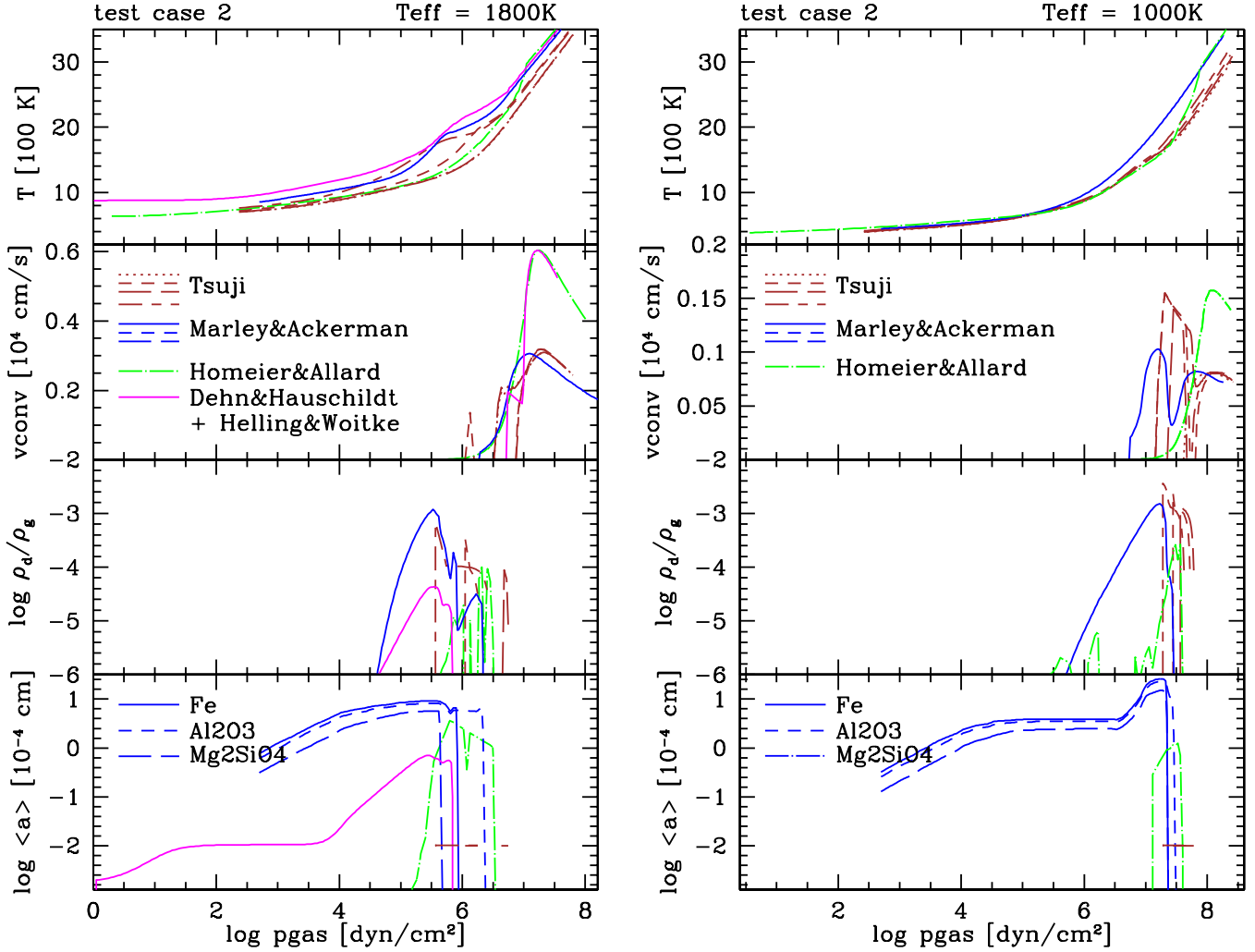


**Figure 5.** Test cases for complete atmospheric models for  $\log g = 5.0$ , solar element abundance with  $T_{\text{eff}} = 1800\text{K}$  (left) and  $T_{\text{eff}} = 1000\text{K}$  (right).

**Note:** Different colours stand for different stellar atmospheres codes. Four models are plotted for the Tsuji-case (brown): long-short-dashed:  $T_{\text{cr}} = 1700\text{K}$  (extended cloud), short-dashed:  $T_{\text{cr}} = 1800\text{K}$ , long-dashed:  $T_{\text{cr}} = 1900\text{K}$  (thin cloud), dotted: no dust opacity considered. Different line styles in  $\log(a)$  indicate different homogeneous dust species in the Marley, Ackerman & Lodders-models.

profiles are much more similar for  $T_{\text{eff}} = 1000\text{K}$  and so is the depth of the absorption features. Consequently, a spectral analysis relying on the depth of near- and IR spectral features, e.g. as gravity indicator, would underestimate the gravity in the case of the Tsuji and the Allard & Homeier-models compared to the Marley, Ackerman & Lodders and Dehn & Hauschildt + Helling & Woitke models in the L - dwarf regime.

It appears that the treatment of the gas-phase opacity can account for some differences in the synthetic spectral energy distribution, here in particular the treatment by the JOLA band method in the Tsuji-models vs. the more frequency sensitive methods used in all other models. However, the completeness of the molecular line lists has only minor effects on our photometry results given the large influence of the dust modelling demonstrated here.

### 3.4.3 Photometric fluxes

We wish to compare our simulations also in terms of photometric fluxes (Figs. 8, 9, 10 and Table 6). We have chosen to demonstrate our comparison for four filter systems covering the near-

IR and the IR: the JHK-2MASS photometric system<sup>6</sup>, the WFCAM UKIRT filters<sup>7</sup>, the IRAC Spitzer photometric bands<sup>8</sup>, and the VISIR VLT system<sup>9</sup>. Delfosse et al. (2000) show for their empirical mass-luminosity relation that model atmosphere results are more reliable in the near-IR (JHK) than at lower wavelength. However, we include the Z and Y (+JHK) from WFCAM UKIRT filter system for comparison. Note that Carpenter (2001) provides transformation formula for the 2MASS colours into a number of different photometric systems (also Hewett et al. 2006).

The Allard & Homeier-model exhibits the highest J, H and Y photometric fluxes in the  $T_{\text{eff}} = 1800\text{K}$ -case, while both Tsuji-models bracket the compared models for the IRAC photometric fluxes (except Band 4). The Allard & Homeier, and the Tsuji- $T_{\text{cr}} = 1900\text{K}$ -models have the largest Y fluxes in the  $T_{\text{eff}} = 1000\text{K}$ -case, and the Tsuji- $T_{\text{cr}} = 1700\text{K}$ -model has the largest flux in Z. The Marley, Ackerman & Lodders-model and the Tsuji- $T_{\text{cr}} = 1900\text{K}$ -

<sup>6</sup> [http://web.ipac.caltech.edu/staff/waw/2mass/opt\\_cal/index.html](http://web.ipac.caltech.edu/staff/waw/2mass/opt_cal/index.html)

<sup>7</sup> <http://www.ukidss.org/technical/technical.html>

<sup>8</sup> [http://ssc.spitzer.caltech.edu/irac/spectral\\_response.html](http://ssc.spitzer.caltech.edu/irac/spectral_response.html)

<sup>9</sup> <http://www.eso.org/sci/facilities/paranal/instruments/visir/inst/index.html>



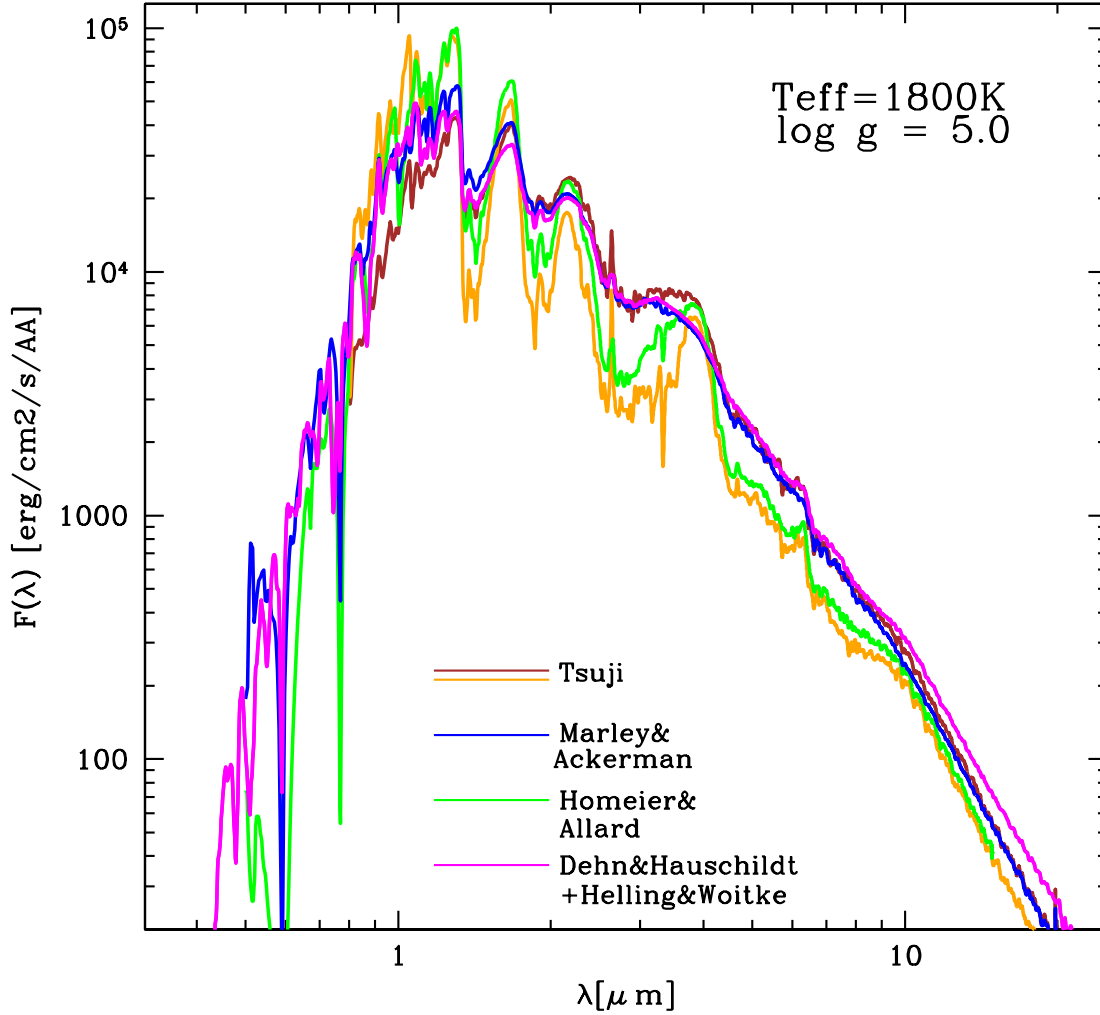


**Figure 6.** Synthetic spectra for  $T_{\text{eff}} = 1800\text{K}$ ,  $\log g = 5.0$  and solar metallicity. Two spectra are plotted for the Tsuji-model:  $T_{\text{cr}} = 1700\text{K}$  (brown; extended cloud) and  $T_{\text{cr}} = 1900\text{K}$  (orange; thin cloud).

model suggest the largest flux in Z for  $T_{\text{eff}} = 1800\text{K}$ . Note that  $\log F_{\text{J}}^{\text{UKIRT}} > \log F_{\text{J}}^{\text{MASS}}$ ,  $\log F_{\text{H}}^{\text{UKIRT}} \approx \log F_{\text{H}}^{\text{MASS}}$ , and  $\log F_{\text{K}}^{\text{UKIRT}} < \log F_{\text{K}}^{\text{MASS}}$  for all model approaches. The model results differ the most in the UKIRT ZYJ bands in both test cases.

Interestingly, the Tsuji models suggest the faintest fluxes in all IRAC band for  $T_{\text{eff}} = 1000\text{K}$  while the Marley, Ackerman & Lodders-models result in the largest fluxes in these wavelength bands. The maximum difference amongst the models in photometric fluxes ( $\Delta_{\text{max}}[\log F_c]$ , last columns Table 6) are larger in the T-dwarf test case than in the L-dwarf test case. The maximum differences occur in the ZYJH bands, and in the VISIR SIV, SiC, and NeII bands for the T-dwarf test case.

These synthetic photometry allows to suggest an error margin due to spread in the model results for apparent magnitudes (definition see Table 1). *The photometric flux differences relate to uncertainties in apparent magnitudes between  $0.25 < \Delta m < 0.875$  for the L-dwarf test case. The uncertainty in apparent magnitudes increases considerably for the T-dwarf test case due to strong differences in the Y band:  $0.1 < \Delta m < 1.375$ .*

Figures 9 and 10 demonstrate how the photometric fluxes of the model atmosphere codes translate into colours (definition see Table 1). For this, we have normalised the photometric fluxes to the corresponding photometric fluxes for Vega ( $\log F_{c0}$  in Tables 1 and 6). The largest differences occur for the L-dwarf model ( $T_{\text{eff}} = 1800\text{K}$ ) in J-[4.5], Ks-[4.5], K-[4.5], and the [3.5]-[4.5]. For the T-dwarf model ( $T_{\text{eff}} = 1000\text{K}$ ) the maximal differences occur in Ks-[3.6], [3.5]-[4.5], and Ks-[4.5].

If we assume the synthetic colours are correct, we can in principle use them to infer the spectral type of an object from an observed (colour, SpT)-diagram<sup>10</sup>. Ideally, the synthetic colours derived in Fig. 9 for  $T_{\text{eff}} = 1800\text{K}$  should result in a L-dwarf and the colours for  $T_{\text{eff}} = 1000\text{K}$  should suggest a T-dwarf. For this exercise, the synthetic colours ( $m_1 - m_2$ ) in Fig. 9 are compared with the observed IRAC colours in Patten et al. (2006), and the related spectral type is picked from their Fig. 10. However, in Patten et al. (2006) the [3.6]-[4.5]-SpT relation appears ambiguous for M7...L8 since

<sup>10</sup> SpT = Spectral Type

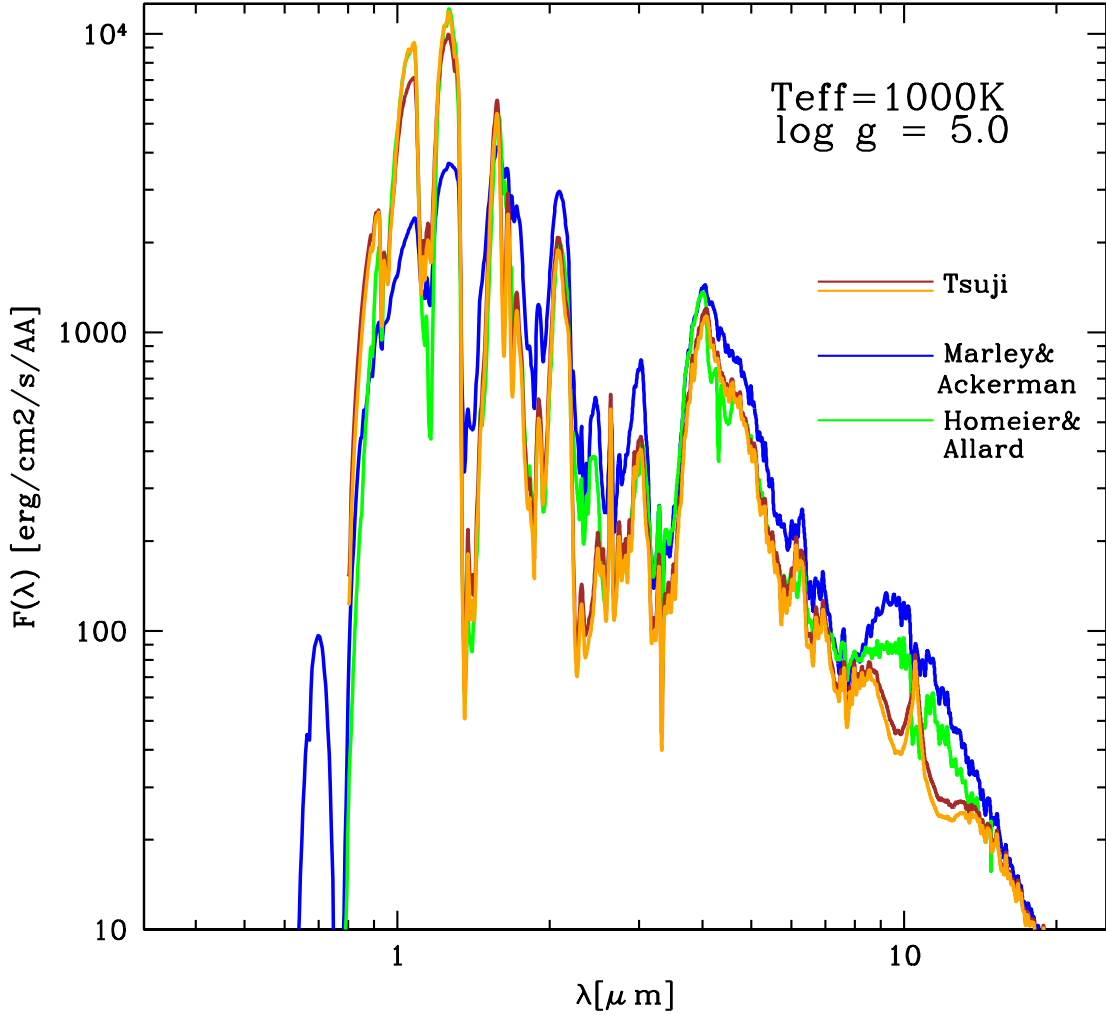


**Figure 7.** Synthetic spectra for  $T_{\text{eff}} = 1000\text{K}$ ,  $\log g = 5.0$  and (initial) solar metallicity. Two spectra are plotted for the Tsuji-model:  $T_{\text{cr}} = 1700\text{K}$  (brown; extended cloud) and  $T_{\text{cr}} = 1900\text{K}$  (orange; thin cloud).

[3.6]-[4.5] remain approximately constant for these spectral types. Our synthetic error margin is slightly larger than the [3.6]-[4.5] scatter in Patten et al. (2006). We encounter a similar challenge in relating our synthetic mean value for [4.5]-[5.8] to a possible spectral type suggesting M0...L7 in the worst case, but the mean value for [4.5]-[5.8] results in SpT= M8...L6. Patten et al. (2006) argue that the scatter in their observed [5.8]-[8.0]-SpT plot might be due to the  $\text{H}_2\text{O}$  vs.  $\text{CH}_4$  absorption at  $7.7\mu\text{m}$ . Our synthetic mean value would then suggest with these observed data an interval of M9...T5 inside the synthetic error bars, while the mean value for [5.8]-[8.0] narrows the SpT range to L0...T4. About the same conservative spectral type range is found for J-[4.5], but can be narrowed to L3...L5 for the J-[4.5]-mean value. For our T-dwarf test case ( $T_{\text{eff}} = 1000\text{K}$ ) the biggest uncertainties in comparison with the Patten et al (2006) data occur for [5.8]-[8.0], Ks-[3.6] and J-[4.5]. However, the SpT-colour relation in Patten et al. (2006) is much narrower for T-dwarfs, and hence, our synthetic mean colours do suggest much narrower SpT ranges than for our L-dwarf test case (compare Table 7).

Interestingly, the two extreme Tsuji-models ( $T_{\text{cr}} = 1700\text{K}$  and  $T_{\text{cr}} = 1900\text{K}$ ) bracket the Y-J and the Z-J UKIRT colours in Fig 10. We compare our synthetic Y-J and J-H UKIRT colours to Hewett et al. (2006), and we reproduce the spectral class of our test case models better than for the near-IR colours (see Table 7). A comparison with Lodieu et al.(2007a) demonstrates that synthetic Z-J colours falls well in their sequence of substellar objects with decreasing mass. However, a proper reproduction of a T-dwarf spectrum would demand an adjustment of cloud parameters like  $T_{\text{crit}}$ ,  $f_{\text{sed}}$  and possibly also the mixing efficiency as described in Sections 2.2.1.2, 2.2.2.2, 2.2.3.4 and 2.2.4.4 compared to the parameter used in this comparison study which are more suitable for L-dwarf model atmospheres (see e.g. Tsuji 2005, Cushing et al. 2008, Stephens et al. 2008).

#### 3.4.4 General

We have evaluated our model results in the most conservative way and despite the differences amongst the simulations in mod-



**Table 6.** Photometric fluxes  $\log F_c$  [erg cm<sup>-2</sup>s<sup>-1</sup>Å<sup>-1</sup>] with c indicating the JHK-2MASS system, the WFCAM UKIRT system, the VISIR-bands, and the IRAC Spitzer bands for the models depicted in Fig. 8. The last column contains the maximum differences in  $\log F_c$  amongst the models:  $\Delta_{\max}[\log F_c] = [\log F_c]_{\max} - [\log F_c]_{\min}$ . Note that Tsuji's thick-cloud case ( $T_{\text{cr}} = 1700\text{K}$ ; each 1st row) is used to calculate  $\Delta_{\max}[\log F_c]$  for the L-dwarf test case ( $T_{\text{eff}} = 1800\text{K}$ ), and Tsuji's thin-cloud case ( $T_{\text{cr}} = 1900\text{K}$ ; each 2nd row) for the T-dwarf test case ( $T_{\text{eff}} = 1000\text{K}$ ). We also list the photometric fluxes for the HST Vega spectrum of Bohlin & Gilliland (2004; Warren 2008, priv. com.) which we use as zero points to calculate the synthetic colours (↗ Table 1; Figs. 9, 10).

Photometric band			Tsuji			Marley, Ackerman, & Lodders		Allard& Homeier		Dehn&Hauschildt +Helling&Woitke		Vega		
c	$\Delta\lambda$ [ $\mu\text{m}$ ]	$T_{\text{cr}}$ [K]	$T_{\text{eff}}$ [K]		$f_{\text{sed}}$	$T_{\text{eff}}$ [K]		$T_{\text{eff}}$ [K]		$T_{\text{eff}}$ [K]		$\Delta_{\text{max}}[\log F_{\text{c}}]$		$\log F_{\text{c}0}$
			1000K	1800K		1000K	1800K	1000K	1800K	1000K	1800K	1000K	1800K	
JHK-2MASS-bands <sup>6</sup> : (■)														
J	1.100 – 1.400	1700	(3.65)	4.46	2		4.62		4.76		4.53		0.30	-1.52
		1900	3.68	(4.72)		3.33		3.65		–		0.35		
H	1.475 – 1.825	1700	(3.34)	4.49	2		4.53		4.62		4.45		0.17	-1.95
		1900	3.28	(4.51)		3.47		3.36		–		0.19		
Ks	2.000 – 2.400	1700	(3.00)	4.35	2		4.29		4.29		4.28		0.07	-2.37
		1900	2.95	(4.14)		3.23		3.02		–		0.28		
ZYJHK-UKIRT-bands <sup>7</sup> :														
Z	0.830 – 0.925	1700	(3.26)	3.87	2		4.22		4.17		4.14		0.35	-1.07
		1900	3.22	(4.39)		2.85		2.94		–		0.37		
Y	0.970 – 1.070	1700	(3.74)	4.31	2		4.50		4.59		4.56		0.28	-1.24
		1900	3.84	(4.78)		3.29		3.84		–		0.55		
J	1.170 – 1.330	1700	(3.86)	4.55	2		4.69		4.89		4.61		0.34	-1.53
		1900	3.90	(4.86)		3.49		3.89		–		0.41		
H	1.490 – 1.780	1700	(3.34)	4.49	2		4.52		4.61		4.44		0.17	-1.94
		1900	3.28	(4.50)		3.45		3.36		–		0.17		
K	2.030 – 2.370	1700	(2.90)	4.34	2		4.27		4.27		4.26		0.08	-2.41
		1900	2.85	(4.11)		3.14		2.94		–		0.29		
IRAC Spitzer-bands <sup>8</sup> : (▲)														
Band 1	2.965 – 4.165 [3.6]	1700	(2.56)	3.90	2		3.81		3.80		3.83		0.10	-3.19
		1900	2.52	(3.66)		2.69		2.70		–		0.18		
Band 2	3.704 – 5.324 [4.5]	1700	(2.85)	3.53	2		3.48		3.36		3.52		0.17	-3.58
		1900	2.83	(3.28)		2.97		2.80		–		0.17		
Band 3	4.626 – 6.896 [5.8]	1700	(2.29)	3.18	2		3.15		2.99		3.20		0.21	-3.99
		1900	2.26	(2.93)		2.45		2.29		–		0.19		
Band 4	5.618 – 10.31 [8.0]	1700	(1.88)	2.72	2		2.71		2.57		2.76		0.19	-4.51
		1900	1.85	(2.50)		2.02		1.95		–		0.17		
VISIR-bands <sup>9</sup> :														
PAH1	8.38 – 8.8	1700	(1.87)	2.61	2		2.59		2.49		2.64		0.15	-4.69
		1900	1.84	(2.43)		2.09		1.93		–		0.25		
ArIII	8.92 – 9.06	1700	(1.80)	2.57	2		2.54		2.46		2.60		0.14	-4.76
		1900	1.76	(2.41)		2.06		1.94		–		0.30		
SIV	10.410 – 10.570	1700	(1.85)	2.36	2		2.32		2.26		2.43		0.17	-5.03
		1900	1.82	(2.23)		1.89		1.65		–		0.24		
PAH2	10.965 – 11.555	1700	(1.52)	2.24	2		2.20		2.16		2.31		0.15	-5.15
		1900	1.46	(2.11)		1.89		1.74		–		0.43		
SiC	10.680 – 13.020	1700	(1.51)	2.17	2		2.13		2.09		2.25		0.16	-5.22
		1900	1.46	(2.04)		1.81		1.66		–		0.35		
NeII	12.695 – 12.905	1700	(1.43)	2.02	2		1.98		1.92		2.10		0.18	-5.37
		1900	1.38	(1.88)		1.66		1.53		–		0.28		
Q1	17.235 – 18.065	1700	(1.03)	1.44	2		1.43		–		1.59		0.15	-5.93
		1900	1.02	(1.31)		1.06		–		–		0.04		
Q2	18.280 – 19.160	1700	(0.94)	1.34	2		1.33		–		1.50		0.17	-6.03
		1900	0.93	(1.22)		0.97		–		–		0.04		
Q3	19.300 – 19.700	1700	(0.85)	1.28	2		1.27		–		1.44		0.17	-6.10
		1900	0.84	(1.15)		0.88		–		–		0.04		

elling clouds, they suggest a general agreement in synthetic colours (Figs. 9, 10). The mean values do provide a good guidance taking into account the large diversity regarding the characteristic cloud quantities like the mean particle sizes and material composition. Of course, uncertainties increase if the error margins given in Table 7

are applied. The values of the spectral types suggested in Table 7 suffers also the scatter and possible ambiguity contained in the observed data like e.g. in the IRAC colours [3.6]-[4.5] or [5.8]-[8.0] as discussed by Patten et al. (2006) which adds to the model inherent uncertainties. A better picture appears if colours are correlated.

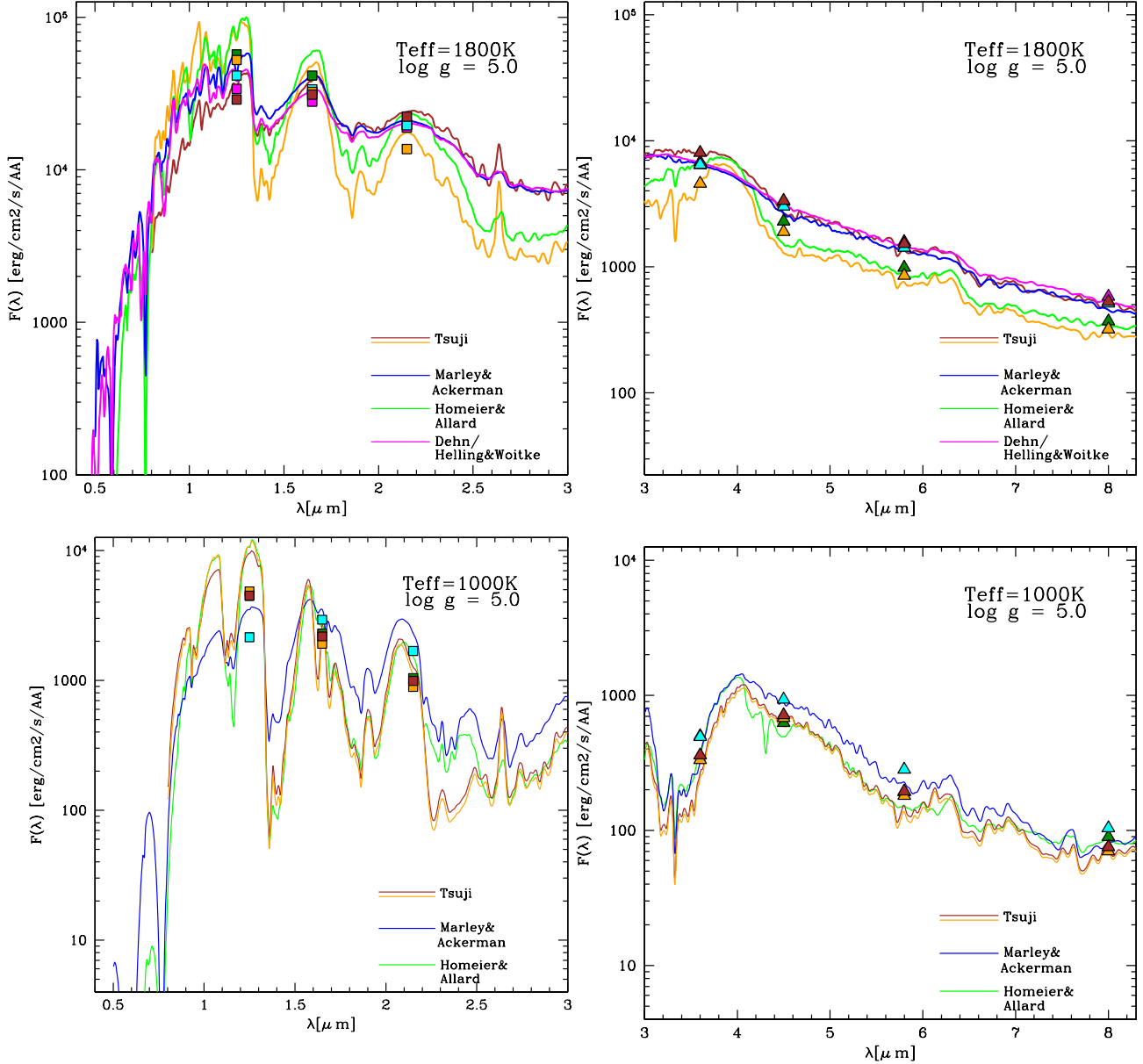


**Figure 8.** Synthetic spectra for  $T_{\text{eff}} = 1800\text{K}$  (top) and  $T_{\text{eff}} = 1000\text{K}$  (bottom) with  $\log g = 5.0$  and solar metallicity for a spectral resolution  $R=200$ . Two spectra are plotted for the Tsuji dust model:  $T_{\text{cr}} = 1700\text{K}$  (brown; extended cloud) and  $T_{\text{cr}} = 1900\text{K}$  (orange; thin cloud). Photometric fluxes (symbols) are plotted for the JHK-2MASS-system (left panels,  $\blacksquare$ ) and the IRAC Spitzer-bands (right panels,  $\blacktriangle$ ) at the band center frequency  $\Delta\lambda/2$ . The photometric fluxes are summarised in Table 6.

A comparison with colour-colour plots (e.g. Lodieu et al. 2007b for UKIRT) shows that the different simulations reproduce well the spectral classes of the test cases even in the most uncertain ZYJ colours. Nevertheless, we refrain from the exercise of back-tracing the  $T_{\text{eff}}$ -values from our synthetic colours since this would clearly potentiate uncertainties because the atmosphere simulations used in publications of interest did not treat the presence of dust at all (in Luhman 1999) or used very simplistic representations of dust as opacity source (in Golomowski et al. 2004).

## 4 DISCUSSION

### 4.1 The challenge of phase-transition modelling

An essential part of modelling clouds in substellar atmospheres is the description of condensation as a phase-transition gas - solid/liquid. Two modelling approaches were used in the simulations compared in this paper: the kinetic approach and the phase-equilibrium approach. Condensation occurs in the kinetic approach when a gas species is supersaturated with respect to its equilibrium concentrate at given pressure and temperature. Homogeneous nucleation of a supersaturated species yields macro-molecules, molecular clusters and eventually nanometer solids. The clusters and nanometer solids could become seeds for heterogeneous nucleation by surface reactions that requires lower activation energies

**Table 7.** Mean synthetic colours ( $(m_1 - m_2)_{\text{mean}} = \sum_L (m_1 - m_2)_L / L$ ;  $L$  - total number of models) and error margins ( $((m_1 - m_2)_{\text{max}} - (m_1 - m_2)_{\text{min}}) / 2$  - maximum colour difference) derived from Figs. 9, 10. The HST Vega spectrum of Bohlin & Gilliland (2004; Warren 2008, priv. com.) is used as zero point. Listed are also the spectral types suggested by the mean synthetic colours alone (each 1st row) and including the synthetic error margin (each 2nd row).

<b>L-dwarf test case (5 models):</b>		
colour	$(m_1 - m_2)_{\text{mean}}^{1800K} \Rightarrow$	SpT <sup>10</sup>
[3.6] - [4.5]	0.0558	$\Rightarrow$ M7...L7
	$0.0558 \pm 0.175$	$\Rightarrow$ M7...T0
[4.5] - [5.8]	0.1662	$\Rightarrow$ M8...L6
	$0.1662 \pm 0.075$	$\Rightarrow$ M0...L7
[5.8] - [8.0]	0.2181	$\Rightarrow$ L0...T4
	$0.2181 \pm 0.040$	$\Rightarrow$ M9...T5
$J - [4.5]$	2.1900	$\Rightarrow$ L3...L5
	$2.1900 \pm 0.175$	$\Rightarrow$ M9...T6
$K_s - [3.6]$	0.8792	$\Rightarrow$ L4
	$0.8792 \pm 0.060$	$\Rightarrow$ L3...L5
$K_s - [4.5]$	0.9349	$\Rightarrow$ L4...L5
	$0.9349 \pm 0.220$	$\Rightarrow$ M0...L7
$Y - J_{\text{UKIRT}}$	$1.141 \pm 0.3$	$\Rightarrow$ L
$Z - J_{\text{UKIRT}}$	$2.557 \pm 0.275$	
$J_{\text{UKIRT}} - H_{\text{UKIRT}}$	$0.513 \pm 0.4$	$\Rightarrow$ L
<b>T-dwarf test case (4 models):</b>		
colour	$(m_1 - m_2)_{\text{mean}}^{1000K} \Rightarrow$	SpT <sup>10</sup>
[3.6] - [4.5]	1.597	$\Rightarrow$ T7.5
	$1.597 \pm 0.2900$	$\Rightarrow$ T7...T8
[4.5] - [5.8]	-0.339	$\Rightarrow$ T7
	$-0.339 \pm 0.0800$	$\Rightarrow$ T7...T7.5
[5.8] - [8.0]	0.317	$\Rightarrow$ L6...T5
	$0.317 \pm 0.1125$	$\Rightarrow$ L6...T6.5
$J - [4.5]$	3.361	$\Rightarrow$ L9...T8
	$3.361 \pm 0.2900$	$\Rightarrow$ L5...T8
$K_s - [3.6]$	0.971	$\Rightarrow$ L4...T4
	$0.971 \pm 0.2750$	$\Rightarrow$ L2...T7
$K_s - [4.5]$	2.568	$\Rightarrow$ T6.5...T7
	$2.568 \pm 0.2000$	$\Rightarrow$ T6.5
$Y - J_{\text{UKIRT}}$	$0.993 \pm 0.175$	$\Rightarrow$ T
$Z - J_{\text{UKIRT}}$	$2.953 \pm 0.400$	
$J_{\text{UKIRT}} - H_{\text{UKIRT}}$	$-0.043 \pm 0.75$	$\Rightarrow$ T

than homogeneous nucleation of the same species directly out of the gas phase. However, the first condensate will form by homogeneous nucleation. A second condensate can form at a lower temperature by heterogeneous nucleation on seeds made of the first condensate or by homogeneous nucleation following supersaturation of the gas. In the phase-equilibrium approach, thermodynamic equilibrium is adopted where the Gibbs energy difference between reagents and products equals zero at fixed values of temperature, pressure and element composition. A series of these calculable states when ordered as a function of decreasing temperature can be viewed as a time sequence of fractional condensation that predicts the stepped appearance of crystallographically ordered, chemically stoichiometric solids, i.e. minerals. Equilibrium condensation models thus predict a sequence of minerals of systematically different compositions. Yet, the presence of a particular mineral or mineral assemblage is no proof of equilibrium condensation.

Laboratory condensation experiments on silicate vapours found that dissipative structures (i.e. metastable states) appear as highly disordered, amorphous solids with unique non-stoichiometric compositions. That is, they have unique Metal-oxide

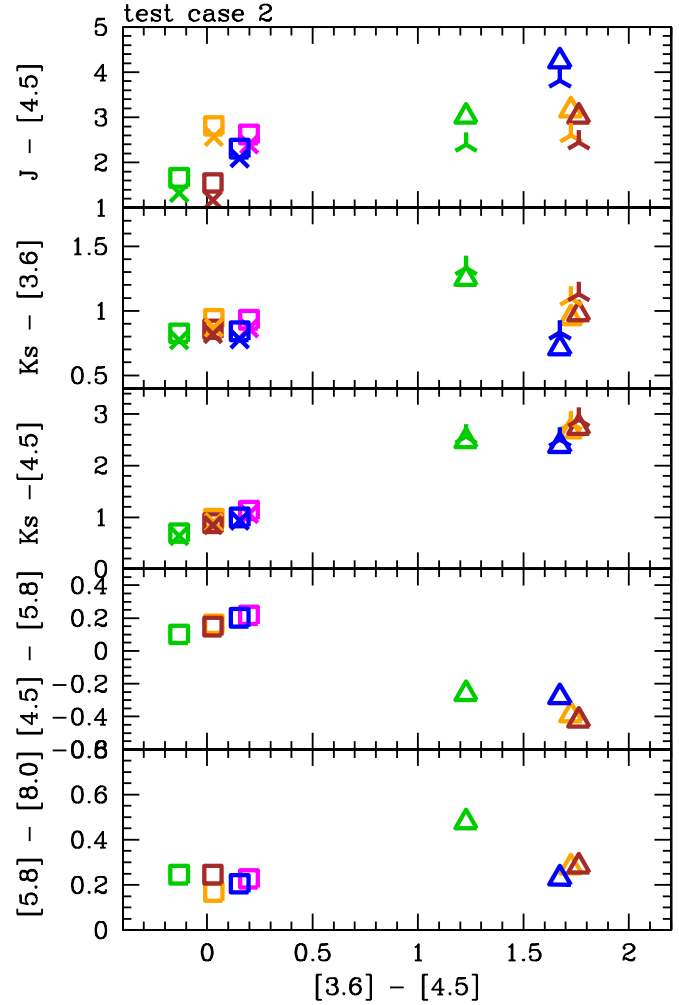


**Figure 9.** Synthetic colour-colour diagrams for 2MASS, for  $T_{\text{eff}} = 1800K$  ( $\square$  and cross) and  $T_{\text{eff}} = 1000K$  ( $\triangle$  and star) with  $\log g = 5.0$  and solar metallicity. The symbol-colour code is the same like in Fig. 6: Tsuji  $T_{\text{cr}} = 1700K$  (brown, thick cloud) and  $T_{\text{cr}} = 1900K$  (orange, thin cloud), Marley, Ackerman & Lodders (blue), Allard & Homeier (green), Dehn & Hauschildt + Helling & Woitke (magenta). The star symbols indicate the colours evaluated for the WFCAM UKIRT filter system.

to  $\text{SiO}_2$  ratios (M: Mg, Fe, Ca, or Al, and combinations thereof) that match deep metastable eutectic compositions in equilibrium phase diagrams (Nuth et al., 1998, 2000; Rietmeijer et al., 1999, 2008). These compositions are intermediate between equilibrium mineral compositions, e.g. serpentine dehydroxylate,  $\text{Mg}_3\text{Si}_2\text{O}_7$ . With time it would break down to forsterite and enstatite ( $\text{Mg}_2\text{SiO}_4 + \text{MgSiO}_3$ ) (Rietmeijer et al., 2002) that both would form at different temperatures during equilibrium condensation. Equilibrium condensation is predictable but so again is extreme non-equilibrium condensation of deep metastable eutectic condensates that are more reactive than equilibrium minerals. With time, post-condensation thermal annealing (i.e. ageing) of non-equilibrium condensates will also lead to thermodynamic equilibrium minerals. Ageing is determined by the prevailing time-temperature regime (Hallenbeck et al., 2000) and condensate morphology, i.e. aggregates or dust clumps (Rietmeijer et al., 1986, 2002). The ageing process will yield minerals at temperatures below their equilibrium condensation temperature. Such processes would require the cloud particles

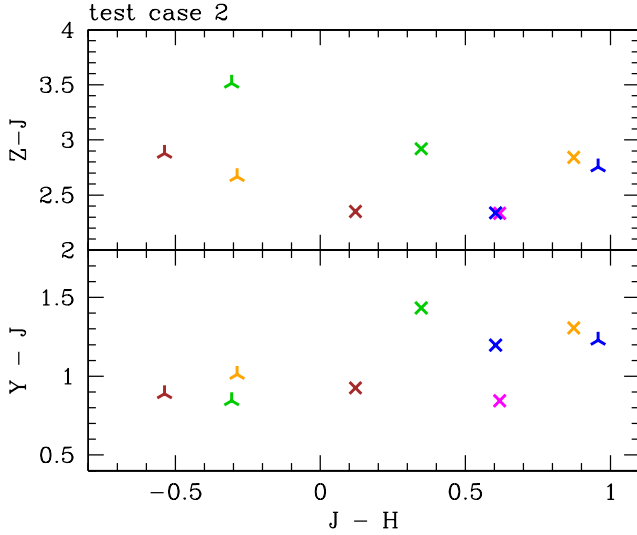


**Figure 10.** Synthetic colour-colour diagrams only for WFCAM UKIRT filters for  $T_{\text{eff}} = 1800\text{K}$  (cross) and  $T_{\text{eff}} = 1000\text{K}$  (star) with  $\log g = 5.0$  and solar metallicity. The symbol-colour code is the same like in Fig. 6: Tsuji  $T_{\text{cr}} = 1700\text{K}$  (brown, thick cloud) and  $T_{\text{cr}} = 1900\text{K}$  (orange, thin cloud), Marley, Ackerman & Lodders (blue), Allard & Homeier (green), Dehn & Hauschildt + Helling & Woitke (magenta).

to remain in a certain thermodynamical state long enough, a situation possibly occurring to dust trapped in-between convection cells.

Toppini et al. (2006) demonstrate that their (Mg,Ca,Al,Si)-oxide vapour condenses to complex hydrates carbonates in a  $\text{CO}_2$ - $\text{H}_2\text{O}$ -rich gas, and they conclude that this condensation proceeds near-equilibrium. Their condensation experiments at moderate gas temperate and low total pressures (1000-1285K, 0.004 bar) yield many of the expected equilibrium condensates in crystalline form. However, both Toppini et al. (2006) and Rietmeijer et al. (2008) conclude that the mineralogy of such condensed material can not be understood without taking into account the influence of kinetics.

## 5 CONCLUSION

Clouds in the atmospheres of brown dwarfs and gas-giant planets determine their spectral appearance and influence their evolution by altering the atmospheric thermal structure. The challenge of modelling cloud formation has been approached from very different perspectives over the past years which leads to the question: Do these models yield the same results and how much do they differ in predicted observational quantities? Five models are compared in this paper to address these questions. All models emphasise the chemistry of cloud formation. Considering clouds as the result of a phase transition process (gas to solid/liquid), the models assuming phase-equilibrium describe the end-state of the phase-transition process, whereas kinetic models describe the initial state of the cloud formation process from a chemical point of view. Which viewpoint is most correct ultimately depends upon the timescales for the various relevant atmospheric processes.

The dust cloud models predict generally comparable cloud structures despite the different approaches, although the results differ substantially in detail. Opacity relevant quantities like grain size, amount of dust, dust- and gas-phase composition vary between the various approaches. Most cloud models agree that small grains composed mainly of silicates ( $\text{MgSiO}_3[\text{s}]/\text{Mg}_2\text{SiO}_4[\text{s}]$ ) populate the upper cloud layers, whereas iron ( $\text{Fe}[\text{s}]$ ) is a major com-

ponent of the large grains at the cloud base. The cloud models agree on the gas-phase composition in the inner atmosphere only which is too warm for condensed phases. All models predict phase-equilibrium here, though the different models describe the evaporation at different levels of detail. Above the cloud, more molecules remain in the gas-phase if cloud formation is treated in phase-non-equilibrium compared to results from phase-equilibrium models. The different results that arise from differences in cloud modelling are amplified if the entire atmosphere problem is solved, including radiative and convective energy transport. The reason is the strong feedback of the clouds on the  $(T, p)$ -structure due to the clouds' strong opacity and its high efficiency in depleting the gas of the atmosphere.

Viewing their spectral appearance, the results of the cloud model atmosphere codes appear to fall into two categories:

- The *high-altitude cloud models* or *extended* (Tsuji  $T_{\text{cr}} = 1700\text{K}$ , Marley, Ackerman & Lodders, Dehn & Hauschildt + Helling & Woitke) where the dust-to-gas ratio peaks at high altitudes though at different absolute levels. In these models, small grains ( $\langle a \rangle = 10^{-6} \dots 10^{-4} \mu\text{m}$ ) are still present well above the maximum of  $\rho_d/\rho_{\text{gas}}$ , hence the gas-phase absorption is less deep for  $\lambda > 1 \mu\text{m}$ .
- The *low-altitude cloud models* or *thin* (Tsuji  $T_{\text{cr}} = 1900\text{K}$ , Allard & Homeier) where the dust-to-gas ratio maximum sits further inside the atmosphere and no grains populate higher atmospheric layers above the maximum of  $\rho_d/\rho_{\text{gas}}$ . Consequently, the gas-phase absorption features are much deeper in the mid-IR and IR part of the spectrum. Consequently, the *low-altitude cloud / thin* model atmospheres appear bluer than the *high-altitude cloud / extended* model atmospheres.

Comparing synthetic photometric fluxes and colours from different model atmosphere codes illustrates the current range of uncertainty, or error bar, for theoretical predictions. These error bars are worst cases. They are derived from a group of different models and not from only one particular family of models. In the most conservative case, the maximum differences in photometric fluxes,  $\Delta_{\text{max}}[\log F_\lambda]$ , amongst the models are between 1% and 30%.  $\Delta_{\text{max}}[\log F_\lambda]$  increases to 50% for the T-dwarf test case in the WFCAM UKIRT wavelength intervals. This translates into an uncertainty in apparent magnitudes for the L-dwarf test case of  $0.25 < \Delta m < 0.875$ .  $\Delta m$  increases to 1.375 for the T-dwarf test case in the WFCAM UKIRT filter system.

We conclude that every comparison with observations should ideally involve models from different groups. This would allow the determination of a synthetic error bar in determinations of fundamental quantities like  $T_{\text{eff}}$ ,  $\log g$ , and metallicity. Ultimately comparison of models to objects with independently constrained properties (from orbital motion and bolometric luminosity, for example) will elucidate the modelling approaches that most accurately capture the relevant physics. Other possibilities for tests include objects in young stellar clusters which have well constrained ages and metallicities.

Future works on cloud formation need to seek more support in laboratory astrophysics. Hydrodynamic modelling of ultra-cool atmospheres will provide the opportunity to study the dynamic processes of cloud formation. They need to including a consistent description of the chemical formation processes and simultaneously address the challenge of a turbulent fluid field.

## ACKNOWLEDGEMENTS

We thank the anonymous referee for the valuable report. ChH thanks Alkes Scholz and Sören Witte for helpful discussions on the manuscript. We thank the participants of the workshop From Brown Dwarfs to Planets: Chemistry and Cloud formation which was supported by the Lorentz Center of the University Leiden, Nederlandse Organisatie voor Wetenschappelijk Onderzoek, The Netherlands research School for Astronomy, the Scottish University Physics Alliance, and European Space Agency.

## REFERENCES

- Ackerman A., Marley M. 2001, ApJ 556, 872  
 Allard F., Hauschildt P.H. 1995, ApJ 445, 433  
 Allard F., Guillot T., Ludwig H.-G. et al. 2003, IAU 211, ed. E. Martin, 325  
 Allard F., Hauschildt P.H., Alexander D.R., Tamanai A., Schweitzer A. 2001, ApJ 556, 357  
 Allard F., Guillot T., Ludwig H.-G., Hauschildt P.H., Schweitzer A., Alexander D.R., Ferguson J.W. 2003, IAU 211, 324  
 Allard F., Allard N. F., Homeier D., Kielkopf J., McCaughrean M. J., Spiegelman F. 2007, A&A 474, L21  
 Allende Prieto C., Lambert D.L., Asplund M. 2002, ApJ 573, 137  
 Anders E., Grevesse N. 1986, *Cosmochim. Acta* 53, 197  
 Asplund M., Grevesse N., Sauval A.J. 2005, APS Conf. Series 336, 25  
 Atreya S.K., Sandel B.R., Romani P.N. 1991, Uranus (A92-18701 05-91), 110  
 Ayres T.R., Plymate C., Keller C.U. 2006, ApJS, 165, 618  
 Barstow M.A., Holber, J.B., Hubeny I., Good S.A., Levan A.J., Meru, F. 2001, MNRAS 328, 211  
 Bishop, J., Atreya, S. K., Romani, P. N., Orton, G. S., Sandel, B. R., & Yelle, R. V. 1995, Neptune and Triton, 427  
 Bohlin R.C., Gilliland R.L. 2004, AJ 127, 3508  
 Burgasser, A. J.,Looper, D. L., Kirkpatrick, J. D., Cruz, K. L., & Swift, B. J. 2008, ApJ, 674, 451  
 Burrows A., Sudarsky D., Hubeny I. 2006, ApJ, 659, 1140  
 Burrows A., Burgasser A.J., Kirkpatrick J.D., Liebert J., Milsom J.A., Sudarsky D., Hubeny I. 2002, ApJ 573, 394  
 Caffau E., Ludwig H.-G., Steffen M., Ayres T.R., Bonifacio P., Cayrel R., Freytag B., Plez B. 2008, A&A, in press  
 Carpenter J.M. 2001, AJ 121, 2851  
 Chase Jr., M.W., Davies C.A., Downey Jr., J.R. et al. 1986, J. Phys. Chem. Ref. Dat., 14(1)  
 Christensen-Dalsgaard J., Di Mauro M.P., Houdek G., Pijper F. 2008, A&A, submitted  
 Cushing M. C., Marley M. S., Saumon D. et al. 2008, ApJ 678(2), 1372  
 Cooper C.S., Sudarsky D., Milsom J.A., Lunine J. I., Burrows A. 2003, ApJ 586, 1320  
 Delfosse X., Forveille T., Ségransan D., Beuzit J.-L., Udry S., Perrier C., Mayor M. 2000, A&A 364, 217  
 Dehn M. 2007, PhD Thesis, University Hamburg  
 Dupuy T.J., Liu M.C., Ireland M.J. 2008, ApJ, in press (arXiv:0807.2450)  
 Fegley B., Lodders K. 1994, Icar 110, 117  
 Ferguson J.W., Alexander D.R., Allard F., Barman T., Bodnarik J.G., Hauschildt P.H., Heffner-Wong A. Tamanai A. 2005, ApJ 623 585  
 Freedman R.S., Marley M.S., Lodders K. 2008, ApJS 174, 71  
 Gail H.-P., Sedlmayr E. A&A 1984, 132, 320  
 Geballe, T., Saumon, D., Golimowski, D. A., Leggett, S. K., Marley, M. S., & Noll, K. S. 2008, Ap. J., submitted  
 Golimowski D.A., Leggett S.K., Marley M.S. et al. 2004, AJ 127, 3516  
 Grevesse N., Noels A., Sauval A.J. 1992, ESA Proc. *Coronal Streamers, Coronal Loops, and Coronal and Solar Wind Composition*, 305  
 Grevesse N., Sauval A.J. 1998, Space Science Review 85, 161  
 Grossman L. & Larimer L. 1974, Revs. Geophys. Space Physics 1, 71-101.  
 Hallenbeck S.L., Nuth III J.A., Nelson R.A. 2000, ApJ 535, 247  
 Helling Ch. 2003, RvMA 16, 115  
 Helling Ch., Dehn M., Woitke P., Hauschildt P.H. 2008a, ApJ 675, L120  
 Helling Ch., Dehn M., Woitke P., Hauschildt P.H. 2008b, ApJ 677, L157 (Erratum)  
 Helling Ch., Oevermann M., Lüttke M.J.H., Klein R., Sedlmayr E. 2001a, A&A 376, 194  
 Helling Ch., Oevermann M., Lüttke M.J.H., Klein R., Sedlmayr E. 2001b, eds. Kozel, Prihoda, Feistauer, 45  
 Helling Ch., Winters J.M., Sedlmayr E. 2000, A&A 358, 651  
 Helling Ch., Woitke P. 2006, A&A 455, 325  
 Helling Ch., Woitke P., Thi W.-F. 2008, A&A, in press (arXiv:0803.4315)  
 Hewett P.C., Warren S.J., Leggett S.K., Hodgkin S.T. 2006, MNRAS 367, 454  
 Iliev I., Ciardi B., Alvarez M.A., Maselli A., Ferrara A., Gnedin N.Y., Mellema G., Nakamoto T., Norman M.L., Razoumov A.O., and 6 coauthors 2006, MNRAS 371, 1057  
 Jeong K.S., Chang Ch., Sedlmayr E., Sülzle D. 2000, J. Phys. B 33, 3417  
 Kleb B., Wood B. 2005, AIAA 2004-2627  
 Lodieu N., Pinfield D.J., Leggett S.K. et al. 2007a, MNRAS 379(4), 1423  
 Lodieu N., Dobbie P.D., Hodgkin S.T. et al. 2007b, MNRAS 380, 712  
 Leggett S. K., Currie M. J., Varricatt W. P. et al. 2006, MNRAS 373, 781  
 Lodders K., Fegley B. 2006, *Chemistry of Low Mass Substellar Objects*, Springer, Heidelberg  
 Lodders K., Fegley B. 1993, *Metic* 28, 387  
 Lodders, K. 2004, ApJ, 611, 587  
 Lodders K. 2003, ApJ 591, 1220  
 Ludwig H.-G., Allard F., Hauschildt P. H. 2002, A&A 395, 99  
 Ludwig H.-G., Allard F., Hauschildt P. H. 2006, A&A 459, 599  
 Luhman K.L 1999, ApJ 525, 466  
 Lunine J.I., Hubbard W.B., Marley M.S. 1986, ApJ 310, 238  
 Marley M.S., Cushing M.C., Saumon D. 2005, ESA SP-560, 791  
 Marley M.S., Gelino C., Stephens D., Lunine J.I., Freedman R. 1999, ApJ 513(2), 879  
 Mihalas, D. 1978, *Stellar atmospheres /2nd edition/* (San Francisco, W. H. Freeman and Co., 1978. 650 p.  
 Moses, J. I., et al. 2004, Jupiter. The Planet, Satellites and Magnetosphere, 129  
 Nuth III J.A., Hallenbeck S.L., Rietmeijer F.J.M. 1998, Earth, Moon, and Planets 80, 73-112  
 Nuth J.A., Rietmeijer F.J.M., Hallenbeck S.L., Withey P.A., Ferguson F. 2000, eds Sitko M.L., Sprague A.L. and Lynch D.K., ASPC 196, 313-332  
 Oppenheimer B.R., Kulkarni S.R., Matthews K., van Kerkwijk M.H. 1998, ApJ 502, 932

- Pascucci I., Wolf S., Steinacker J., Dullemond C.P., Henning Th., Niccolini G., Woitke P., Lopez, B. 2004, A&A 417, 793
- Patten B.M., Stauffer J.R., Burrows A. et al. 2006, ApJ 651, 502
- Patzner A.B.C., Chang Ch., Sedlmayr E., Sülzle D. 2005, Eur.Phys.J.D 32, 329
- Rietmeijer F.J.M, Nuth J.A., Mackinnon I.D.R. 1986, Icarus 65, 211-222.
- Rietmeijer F.J.M., Nuth III J.A., Karner J.M. 1999, ApJ 527, 395-404
- Rietmeijer F.J.M., Hallenbeck S.L., Nuth III J.A., Karner J.M. 2002, Icarus 156, 269-286.
- Rietmeijer F.J.M., Pun A., Kimua Y., Nuth III J.A. 2008, Icarus 195, 493-503
- Rossow W.B. 1978, Icarus 36, 1
- Rotundi A., Brucato J.R., Colangeli L. et al. 2000 Meteoritics & Planet. Sci. 37, 1623-1635.
- Röllig M., Abel N.P., Bell T., Bensch F., Black J., Ferland G. J., Jonkheid B., Kamp I., Kaufman M.J., Le Bourlot J., and 14 coauthors 2007, A&A 467, 187
- Saumon D., Marley M. S., Cushing M. C., Leggett S. K., Roellig T. L., Lodders, K., Freedman, R. S. APJ 2006, 647, 552
- D. C. Stephens, S. K. Leggett, D. Saumon et al. 2008, ApJ, submitted
- Tsuji T., Ohnaka K., Aoki W., Nakajima T. 1996b, A&A 308, L29
- Tsuji T., Ohnaka K., Aoki W. 1996a, A&A 305, L1
- Tsuji T. 1973, A&A 23, 411
- Tsuji T. 2000, eds. R. Rebolo and M. R. Zapatero-Osorio, 156
- Tsuji T. 2005, ApJ 621, 1033
- Tsuji T. 2002, ApJ 575, 264
- Visscher et al. 2006, ApJ 646, 1181
- Vrba F.J., Henden A.A., Lugnibuhl C.B. et al. 2004, AJ 127, 2948
- Woitke P., Krüger D., Sedlmayr E. 1996, A&A 311, 927
- Woitke P., Helling Ch. 2003, A&A 399, 297
- Woitke P., Helling Ch. 2004, A&A 414, 335